Coupled Ensemble Data Assimilation for Global Oceanic Climate Studies, Part I: System Design and Evaluation

S. Zhang*, M. J. Harrison, A. Rosati, A. Wittenberg

Geophysical Fluid Dynamics Laboratory, Princeton University

Princeton, NJ 08542, USA

(submitted to MWR)

* *Corresponding author address:* Shaoqing Zhang, GFDL/NOAA, Princeton University, P.O. Box 308, Princeton, NJ 08542, USA. Email: Shaoqing.Zhang@noaa.gov Tel: (609)452-6540 Fax: (609)987-5063

ABSTRACT

A fully-coupled data assimilation (CDA) system, consisting of an ensemble filter applied to GFDL's global fully-coupled climate model (CM2), has been developed to facilitate the detection and prediction of seasonal-to-multidecadal climate variability and climate trends. The assimilation provides a self-consistent, temporally-continuous estimate of the coupled model state and its uncertainty, in the form of discrete ensemble members which can be used directly to initialize probabilistic climate forecasts. Here we evaluate the CDA using a series of perfect-model experiments, in which a particular 20th-century simulation – with temporally-varying greenhouse gas and natural aerosol radiative forcings – serves as a "truth" from which observations are drawn, according to the actual ocean observing network for the 20th century. These observations are then assimilated into a coupled model ensemble that is subjected only to pre-inductrial forcings. By examining how well this analysis ensemble reproduces the "truth," we then assess the skill of the analysis system in recovering anthropogenically-forced trends and natural climate variability, given the historical observing network.

The assimilation successfully reconstructs the 20th-century ocean heat content variability and trends in most locations. The experiments highlight the importance of maintaining key physical relationships among model fields, which are associated with water masses in the ocean and geostrophy in the atmosphere. For example, when only oceanic temperatures are assimilated, the ocean analysis is greatly improved by incorporating the temperature-salinity covariance provided by the analysis ensemble. Interestingly, wind observations are more helpful than atmospheric temperature observations for constructing the structure of the tropical atmosphere; the opposite holds for the extratropical atmosphere. The experiments indicate that the Atlantic meridional overturning circulation is difficult to constrain using the 20th-century observational network, but there is hope that additional observations – including those from the newly-deployed Argo profiles – may lessen this problem in the 21st century. The challenges for data assimilation of model systematic biases and evolving

observing systems are discussed.

1 Introduction

A numerical coupled model system that describes the interactions between the atmosphere, land, ocean and sea-ice contains uncertainties. The uncertainties can be attributed to incomplete understanding of radiative effects of various components of the earth system that are simulated, and inaccurate numerical implementation of physical processes such as clouds, radiation, convection and turbulent mixing etc. Therefore, the coupled model system can be viewed as a continuous stochastic dynamical process (instead of a single deterministic process), in which the climate evolution is described by a vectorized stochastic differential equation (Jazwinski, 1970),

$$d\mathbf{x}_t/dt = \mathbf{f}(\mathbf{x}_t, t) + \mathbf{G}(\mathbf{x}_t, t)\mathbf{w}_t \tag{1}$$

Here, $\mathbf{x}_t$ is an n-dimensional vector representing the coupled model state at time t (n is the size of the model state), $\mathbf{f}$ is an n-dimensional vector function, $\mathbf{w}_t$ is a white Gaussian process (uncorrelated in time) of dimension r with mean 0 and covariance matrix $\mathbf{S}(t)$ while $\mathbf{G}$ is an $n \times r$ matrix. The first and second terms of the right hand side in Eq. (1) respectively represent the deterministic modeling and uncertainty contributions in a coupled system.

These uncertainties lead to the existence of the modeled climate drifts from the real world. On the other hand, observations on climate state variables are sparse and noisy in both time and space. For example, the expendable bathythermograph (XBT), the major means of measuring the ocean state throughout the 20th century, provides basically only temperature profiles based on irregular ship courses; and starting from the early of 1990's, satellite measurements began to provide the changes of sea surface heights (SSH), i.e. altimetry data. All observations have instrument measurement errors and sampling (representation) errors. Neither modeling nor observations alone provide a complete picture of climate variations (which in oceans are defined by the time series of 3-dimensional temperature, salinity and currents etc.).

Climate research requires the implementation of data assimilation with coupled climate

models for 1) assessment of climate change from all perspectives (e.g. see Hahn and Manabe 1982), 2) initialization of forecasts (Rosati et al. 1997) and 3) estimation of climate state components for which adequate measurements are still unavailable. Coupled data assimilation (CDA) uses ocean-atmosphere coupled dynamics to extract the signals from available observations (some aspects of climate states during some time periods) to produce a continous timeseries of climate states in which each variable is distributed over a regular mesh in time and space. Coupled dynamics impact the assimilation results in both direct and indirect ways. The direct way refers to using observations to directly adjust certain exchange fluxes between coupled components using covariances between fluxes and observed variables. Examples include that wind stresses and heat/water fluxes at the ocean surface are adjusted by the observed temperature at the top of the ocean. On the other hand the assimilation results can be impacted indirectly by the feedback processes between coupled components, which improve the estimate of the background covariances in the assimilation. One example is when only oceanic data assimilation (ODA) is carried out in a CDA system in which the atmospheric circulations shall be improved by the corrected sea surface temperature (SST) and in return the improved atmospheric flows provide better surface fluxes to the oceans so as improving the estimate of the background covariance in ODA. This positive feedback process shall speed up the convergence of assimilation and enhance the assimilation quality. Combining all aspects above, the net result is that the reconstructed historical sequence of climate states by CDA blends the observational information and coupled dynamics. Since all components of the CDA-estimated coupled model state are expected to stay in a dynamical balance at any instant in time, the initial shock of coupled model forecasts initialized from CDA products is expected to be minimized.

The coupled data assimilation system at GFDL (Geophysical Fluid Dynamical Laboratory, NOAA) solves for a temporally-varying probability density function (PDF) of climate state variables by combining the PDF of observations and a prior PDF derived from dynamically-coupled models using the framework described by Eq. (1). The gained temporally-varying PDF is a complete solution for the coupled data assimilation problem. The climate

state is estimated by the expectation (the first moment of the PDF, i.e. the ensemble mean) and the uncertainty of the estimate is measured by all higher order moments. The vectorized Eq. (1) means that the solved PDF has a joint-distribution nature that reflects the physical balance between state variables required by the coupled model dynamics. The prior PDF is discretely estimated using a set of ensemble integrations of the coupled model by a Monte Carlo approach. The combination of the observational PDF and the prior PDF is implemented using the ensemble adjustment Kalman filter (EAKF, Anderson 2001; 2003). Since four major components in the GFDL's coupled climate models – atmosphere model, land model, ocean model and sea-ice simulator – are highly parallelized, the ensemble filter, also serving as the ensemble organizer, involves a so-called super-parallel technique, which is an extension from the previous study of Zhang et al. (2005). The system is currently configured for assimilating both atmospheric and oceanic observations. Under the same ensemble organizer and filter framework, other assimilation components (land and sea-ice, for instance) can be added feasibly in the future when the relevant measurements for assimilation become available. Utilizing the cross-covariances provided by the joint-PDF of climate state variables, evaluated by the ensemble integrations, the system is able to maintain the physical balance (relying on the ensemble size according to the availability of computation resources) between different climate state variables. Thus, it has a wide scope of applications.

For multiple purposes such as climate detection, ocean observing system evaluation and assimilation validation etc., as the first step of the CDA system application this study and the follow-up one (Zhang et al. 2006) are using a perfect model study framework, or called idealized 'twin' experiments. The truth in the twin experiments is a long model integration with the temporally-varying green house gas (GHG) and natural aerosol (NA) radiative forcings. The 'observations' are the projections of the truth onto a certain observational network, imposed by white noise to simulate the observational errors. Under the perfect model study framework, the CDA system has completed a series of long (25 years) assimilation experiments based on the 20th century (XBT, CDT... etc) and 21st century (Argo) ocean observational networks. This study focuses on the system description and the first

step validation. In particular two test cases are examined to illustrate the importance of maintaining geostrophic balance in atmospheric data assimilation (ADA) and maintaining the temperature-salinity (T-S) relationship in oceanic data assimilation (ODA). The most difficult assimilation case in the series of ODA experiments, uses a fixed-year GHGNA radiative forcing to retrieve the truth (from a simulation with the temporally-varying GHGNA radiative forcings) through the XBT network. Its analysis serves as a preliminary evaluation of the system. Detailed analyses and diagnostics about the impact of the XBT/Argo ocean observational network, the temporally-varying GHGNA radiative forcing in assimilation and the atmospheric data constraint on climate detection will be presented in follow-up studies.

This study is organized as follows: Section 2 describes the coupled model and filtering algorithm with parallelization design. Section 3 describes twin experiment design. Section 4 examines the importance of maintaining the T-S relationship in oceanic data assimilation. Here the importance of assimilating salinity data for estimating climate states, based on a dummy salinity observing network, is also discussed. Section 5 examines the importance of maintaining geostrophic balance in reconstructing the mid- and high-latitude atmospheric structure. Section 6 analyses and discusses the results of a long ODA experiment, which provides a preliminary evaluation of the system. Summary and discussions are given in section 7.

2 Description of coupled data assimilation system

2.1 GFDL's coupled climate model: CM2

Using both the B-grid finite difference and finite-volume atmosphere dynamical cores, GFDL has two coupled climate models: CM2.0 and CM2.1. For convenience of Massive Parallel Processing (MPP) design of the ensemble filter, the B-grid version (CM2.0) is first chosen to implement the coupled data assimilation. The CM2.0 uses the GFDL atmosphere model AM2p12 (AM2/LM2, GAMDT 2005) with a B-grid dynamical core that has 24 vertical levels and 2.5° longitude by 2° latitude horizontal resultion, including a Mellor-Yamada 2.5

dry planetary boundary layer, relaxed Arakawa-Schubert convection and a simple diffusive parameterization of the vertical momentum transport by cumulus convection.

The ocean component is the fourth version of Modular Ocean Model (MOM4) configured with 50 vertical levels (22 levels of 10 m thickness each in the top 220 m), $1^\circ \times 1^\circ$ horizontal B-grid resolution telescoping to $1/3^\circ$ meridional spacing near the equator. The model has an explicit free surface with true freshwater fluxes exchanged between the atmosphere and ocean. Parameterizations include KPP vertical mixing, neutral physics, a spatially-depedent anisotropic viscosity, a shortwave radiative penetration depth that depends on a prescribed climatological ocean color. Insolation varies diurnally and the wind stress at the ocean surface is computed using the velocity of the wind relative to the surface currents. An efficient time-stepping scheme (Griffies 2005) is employed. More details can be found in Gnanadesikan et al. (2005) and Griffies (2005).

The sea-ice component of CM2.0x is the GFDL Sea Ice Simulator (SIS), a dynamical ice model with three vertical layers (one snow and two ice) and five ice-thickness categories. The elastic-viscous-plastic technique (Hunke and Dukowicz 1997) is used to calculate ice internal stresses, and the thermodynamics is a modified Semtner three-layer scheme (Winton 2000). More details can be found in Appendix 1 of Delworth et al. (2005). The interactions of these four major model components in the GFDL's coupling system are schematically demostrated in Fig. 1.

2.2 Ensemble adjustment Kalman filter under a local least squares framework

The general derivation of an ensemble filter from the Bayes's rule (Jazwinski, 1970) can be found in the literature (e.g. Evensen, 1994; Miller et al., 1994,;1998; 1999; Houtekamer and Mitchell, 1998; 2001; Burgers et al., 1998; Van Leeuwen, 1999; Mitchell and Houtekamer, 2000; Bishop et al., 2001; Hamill et al., 2001; Anderson, 2001; Whitaker and Hamill, 2002). Tippett et al. (2003) analyzed existing ensemble-based filters (Anderson, 2001; Bishop

et al., 2001; Whitaker and Hamill, 2002) and pointed out that these methods are roughly equivalent and suggested that the deterministic square root filter (Andrews, 1968) as a unified family name may be appropriate. Houtekamer and Mitchell (2001), Anderson (2003) pointed out that ensemble-based filters can be applied sequentially to individual scalar observations when each scalar observation has an independent error distribution, or with the application of a singular value decomposition technique when the observational errors are correlated (Anderson, 2003). Furthermore, Anderson (2003) described a two-step data assimilation procedure for ensemble filtering under a local least squares framework, which is quite suitable for applying to implementation of parallelization if an appropriate core domain and halo size is defined (Zhang et. al 2005). Without mathematical details, but with the aid of a schematical diagram as shown as Fig. 2, a detailed flow for the two-step assimilation procedure is depicted: the first step computes ensemble increments at an observation location and the second step distributes the increments over the impacted grids. This universal algorithm is applied to the atmospheric data assimilation (ADA, sections 5) and oceanic data assimilation (ODA, section4) with their own parameters according to the different time scale and internal variability in atmospheric/oceanic processes for constructing the GFDL's CDA system.

The two-step procedure first computes the ensemble increment at the observation location produced by an observation available, y with the observation value y^o and standard deviation σ_y^o, which has a Gaussian distribution (marked by the thick-dashed arrow "STEP1"). Then a least square fit is used to distribute the increment over the relevant grid points (marked by the thick-dashed arrow "STEP2") for each ensemble member. The reshape (solid arrow 1) of the prior PDF at the observation location denotes the formation of the new ensemble spread, ($\Delta y^{'}$ as below, dotted curve in right-bottom panel) from the prior ensemble spread (Δy^p as below, solid-thin curve) by the observation distribution (denoted by "obs PDF"). $\Delta y_i^{'}$ is formulated by

$$\Delta y_i^{'} = \frac{\Delta y_i^p}{\sqrt{1+r_k^2}} \tag{2}$$

$$r_k = \frac{\sigma_{k,k}^p}{\sigma_{k,k}^o} \tag{3}$$

where i represents the ensemble sample index and k represents the observation index, $\sigma_{k,k}^o$ and $\sigma_{k,k}^p$ represent the standard deviation of the observation error and its prior estimate from the ensemble, respectively. r_k is the ratio of the estimated prior ensemble standard deviation and the observational error standard deviation. Eq. (3) says that if the estimated prior ensemble variance is greater than the observational error variance ($r_k > 1$), the ensemble spread is largely reduced by the observation, and otherwise the ensemble stays close to the prior. The shift of ensemble mean (solid arrow 2) induced by this observation is computed by

$$\overline{y}^u = \frac{\overline{y}^p}{1+r_k^2} + \frac{y^o}{1+r_k^{-2}}. \tag{4}$$

(4) shows that if the estimated prior ensemble variance is greater than the observational error variance, the ensemble mean shifts towards the observation value, and otherwise the ensemble mean stays close to the prior. Then, the increment induced by the observation y^o for the i-th ensemble sample member at the observation location is

$$\Delta y_i^o = (\overline{y}^u + \Delta y_i^{'}) - y_i^p. \tag{5}$$

Once the ensemble increments at the observation location are available, a least square fitting is applied to distribute the increments onto all gridpoints impacted by the observation using the covariance between the gridpoint (j) and the observation location (k), $c_{j,k}^p$, as

$$\Delta x_{i,j} = \frac{c_{j,k}^p}{\sigma_{k,k}^p} \Delta y_i^o \tag{6}$$

where x represents the component of certain state variable at gridpoint j. The computation in Eq. (6) (marked by solid arrow 3) uses the ensemble-estimated covariance between the observation location and the model gridpoint, $c_{j,k}$, denoted by the shaded region around observation location (asterisk) and model gridpoint location (circle) to distribute the observation increments Δy_i^o onto all relevant gridpoints for each ensemble sample member so that an "analysis PDF" is formed (left panel). This kind of ensemble-based algorithm is sequential since the prior ensemble estimate of any observation, which is used to compute $\sigma_{k,k}^p$, $c_{j,k}$, y_i^p and $\overline{y}^p$ in (3)–(6), is updated using the ensemble vector adjusted by what is already known. The background covariance is a function of time and space, i.e., it is flow-dependent and anisotropic.

As shown above, an ensemble filter uses finite samples to estimate the probability density function (PDF) of a state variable, solving the data assimilation problem by computing the product of modeled and observational PDFs. This process called *filtering* solves for siginals that have major likelihood at the center of PDF and gets rid of noise with minor likelihood at the tails of PDF; it uses a linear regression based on error covariance between the analysed and observed variables (as illustrated in Fig. 2). In an ensemble-based filtering algorithm, the background error covariance between state variables is directly computed from the model ensemble integrations by a Monte Carlo approach. It is convenient to conduct multi-variate data assimilation using an ensemble filter since once error covariances are available, the observational increment of any variable if available can be regressed onto another to obtain the adjustment amount. The nature of multi-variate adjustment is essentially important for solving such problems as climate assessment that require maintenance of the joint-distribution as much as possible. The other important advantage of ensemble-based filters is that error covariances used in regression are flow-dependent and temporally-varying (Zhang and Anderson 2003). Thus, they are well-suited to handle the nonstationary stochastic processes like climate variations in which flow structures are highly anisotropic and strongly dependent on the seasonal cycle and interannual fluctuations.

2.3 A 'super'-parallelized ensemble filter with CM2

Given the fact that, due to the limitation on memory storage, a single GFDL's coupled model run requires a parallel computation environment [a minimum number of Processing Elements (PEs) is 20 on the SGI Intel-Altix cluster, for instance] the ensemble filter demands a so-called "super-parallelization" technique to guarantee that model ensemble integrations and the filtering computation are conducted iteratively online. First, a large number of PEs (say K is the total PE number) are loaded and re-grouped to form a global PE list and M sub-PE-lists each of which has K/M PEs (where M is the ensemble size). The analysis domain decomposition gets done on the global PE list in which K analysis domains (each containing a core domain and a halo, Zhang et al. 2005) are formed. Within each sub-PE-list, the model domain decomposition is first conducted and a certain ensemble member model integration is then advanced in parallell, in which each PE works for a sub-domain. In this process, these M sub-PE-lists work independently and the whole ensemble of model integrations is forwarded synchronously. Then, when model ensemble reaches an observational time, a data transfer process from the model domains (sub-PE-lists) to the analysis domain (global PE list) is activated so that an ensemble vector is formed in each analysis domain where a specific PE updates the ensemble vector by assimilating observations independently. Once the analysis process is done, data in the ensemble vectors over core domains are transferred back to model domains for each ensemble member on a certain sub-PE-list for initializing the next cycle of ensemble model integrations. A flow-chart illustrating the iterative procedure specifically for a 6-member ensemble is shown in Fig. 3 in which each member uses 30 PEs to carry out the model integration (left panels) while the daily filtering analysis uses 180 PEs (right panels).

3 Design of a perfect model study using the existing ocean observational network

3.1 Perfect model framework

Coupled data assimilation is a multi-task problem that involves many issues: coupled model bias, sampling of the observing system, validation of the analysis scheme, etc. A CDA system is so complex that any uncertainty in those aspects described above may cause the evaluation of CDA results to become extremely difficult. To reduce the complexity, this study excludes the model bias issue by using a perfect model study framework, or called identical twin experiments, in which a real ocean observational network is used to sample a modeled timeseries of climate states serving as the true solution of the assimilation problem. Then it is feasible to evaluate the assimilation quality by verifying assimilation results with the "truth" so that any upgrade/degrade of assimilation system, when a new assimilation component or observational data type is added, or, an assimilation parameter is tuned, can be quantified. Once confidence in the assimilation scheme of a CDA system is established, how much an observing system contains the signal of climate variations can be evaluated by verifying assimilation results based on the observational network with the truth. This process within the identical twin framework is referred to as observing system simulation experiment (OSSE), or called climate detection since various scale variability and trend in climate variations have to be assessed in this process. The perfect model framework that is designed in this study is based on the real ocean observational network which is important not only for the CDA system developement but also for OSSEs/climate detection.

3.2 Idealized 'observed' data on the actual ocean observational network

In this study, all observed ocean data are produced by projecting a model integration onto a real observational network and superimposing white noise. The 3-dimensional structure of the ocean observational network is based on the temperature profiles taken from World Ocean

Database (WOD) maintained by National Oceanographic Data Center (NODC). Data types used here mostly are the same as used by Levitus et. al (Levitus and Boyer 1994; Levitus and Antonov 1997; Levitus et al. 2000, Levitus et al. 2005) for World Ocean Analysis (WOA) including Expendable Bathythermograph (XBT), Conductivity-Temperature-Depth (CTD), Drifting Buoy (DRB), Ocean Station Data (OSD), Undulating Oceanographic Recorder (UOR) and Moored Buoy (MRB), shown in Fig. 4. The GFDL's IPCC (Intergovernmental Panel on Climate Change) 20th century historical integration that uses the temporally-varying greenhouse gas (GHG) and natural aerosol (NA) radiative forcings is set to be the true solution for the assimilation experiments. Then the observed ocean profiles are formed by sampling the historical integration temperature and/or salinity data from the ocean observational network on a daily basis, and adding white noise. The projection from the model space onto the observational space is basically a tri-linear (horizontal and vertical) interpolation. The imposed white noise attempts to account for random measurement errors of the observing system and the interpolation error in projection. The standard deviation of the white noise is 0.5°C for temperature and 0.1 PSU for salinity at the sea surface (typical error levels for SST and sea surface salinity, SSS) and exponentially decays to zero at 500 m depth. The representation errors of the observations, which reflect the limitation of the scales of observation sampling, are not included in the superimposing white noise. How to realistically construct the error distribution to represent sampling errors could be an interesting research topic in itself.

3.3 'Observed' data for the atmosphere

The atmospheric observations take the monthly mean reanalysis format (i.e. grid point values) of atmospheric variables (full gridpoints) in the GFDL's IPCC historical run described before. In this case, an observed atmospheric variable is a monthly mean timeseries from the model integration, to which white noise is superimposed with standard deviations of 1 °C for temperature, 1 m/s for u, v and 10 hPa for surface pressure. Again those numbers represent typical standard deviation values of atmospheric observational errors that do not

include the representation error of observations.

As discussed under equation (4) in section 2.2, the standard deviation of observational errors is a parameter which determines the strength of the observational constraint. The values of the atmospheric observation error standard deviation set in this section and the values of the oceanic observation error standard deviation set in the last section may be tuned for an optimal observational constraint.

4 Tests on oceanic data assimilation (ODA)

The ocean observational network from the last quarter of the 20th century is used to sample the GFDL's IPCC historical run. All assimilation experiments in this study use observed ocean data only above 500 m. A totally independent ensemble initial condition is formed by combining the atmosphere and land states at 00UTC 1 January of years 0041, 0042, 0043, 0044, 0045 and 0046 with the ocean and ice state at 00UTC 1 January 0044 of the GFDL's IPCC control run (using the 1860 fixed-year GHGNA radiative forcing). The assimilation model integration only uses the fixed-year GHGNA radiative forcing at 1860, which is the hardest assimilation case in perfect model study since the different GHGNA radiative forcing in the truth and in the assimilation model may introduce the model bias into the assimilation. The initial motivation to use fixed-year GHGNA radiative forcing in the assimilation model attempts to find out how much of the radiative forcing information is detectable by an ocean observational network, although the temporally-varying GHGNA radiative forcing shall be used in real data assimilation. The impact of the temporally-varying GHGNA radiative forcing on data assimilation for climate detection and ocean observing system evaluation shall be discussed in an accompanying study (Zhang et al. 2006), where the assimilation results with the fixed-year/temporally-varying GHGNA radiative forcing are compared and analysed in detail. Then all ODA tests shown below try to anwser the following question: By sampling the ocean observational network how much can we retrieve of the truth? In other words these tests offer a means of simultaneously evaluating the assimilation system

and the ocean observing system.

4.1 Importance of maintaining the T-S relationship

Given the fact that most ocean observations in the 20th century consist of temperature only, once the oceanic data assimilation (ODA) system using the GFDL's coupled climate models is set up, the first issue we want to address is the capability of the ODA system to maintain the physical balance in ocean flows, mostly characterized by the T-S relationship, while assimilating only ocean temperature data. As shown in Fig. 4, from the 1970's to the 1990's the coverage of the ocean observational network had improved. We chose 1991 as a representative sample in the 1990's coverage for this first set of tests. Most of parameters in the ODA scheme are the same as in Zhang et al. (2005) except for those that need to be adjusted according to the new model configuration such as the halo size (10^o for both longitude and latitude) and the time window (2 days before and after the analysis time). In addition, the correlation scale [the parameter a in $\Omega(a,d)$] is multiplied by a $cos\phi$ (ϕ is the grid latitude) factor to make the scale consistent with the character of the Rossby deformation radius for a global analysis scheme. The vertical a is set to be the width of a grid box (10 m above 200 m and it gradully increases up to 80 m arround the 500 m depth) and each observation is only allowed to impact at most four neighboring levels (two above and two underneath).

Figures 5 and 6 are plots of the annual mean ocean potential temperature (hereafter just referred to as temperature for simplicity, unless otherwise noted) and salinity errors averaged over top 500 m. Allowing the observed temperature to only correct the temperature itself (the literature refers this as a univariate analysis scheme) denoted by T2T in panel b of Fig. 5, the ODA process reduced the top ocean temperature error (root mean square, RMS) by 45% (from 0.8139 to 0.4549) compared to the control case (without any data constraint, panel a in Fig. 5). However, the univariate scheme increases the salinity error by 7% (panel b in Fig. 6) compared to the control case (panel a in Fig. 6). From the zonal-depth

sections of temperature (Fig. 7) and salinity (Fig. 8) errors at the equator, it is found that the assimilation of temperature causes the top 250 m of the central Pacific Ocean to cool (comparing panel *b* to panel *a* in Fig. 7) since data require a relatively shallow tharmocline while the west Pacific Ocean becomes too fresh (comparing panel *b* to panel *a* in Fig. 8). The T-S imbalance in the univariate assimilation scheme also causes larger salinity errors in other places such as the Atlantic and Indian oceans. The following example investigates how temperature and salinity errors can both be coherently reduced over the tropical Pacific by employing the T-S covariance.

The cooling of the central Pacific caused by the assimilation of oceanic temperature can be clearly exhibited in the zonal-depth distribution of the temperature correction right at the equator (panel *a* in Fig. 9). Yet the positive T-S covariance over the central Pacific (panel *b* in Fig. 9) means that in order to satisfy simultaneously the model relationship as well as the cooling response, the ocean has to be fresher. Since the salinity remains unadjusted in the univariate assimilation scheme, the water's density in the central Pacific Ocean is higher than it should be. This higher density causes excessive downwelling (panel *b* of Fig. 10) over the central Pacific. Through the same mechanism, excessive upwelling is produced in the western Pacific by the univariate assimilation scheme, due to the failure to maintain the correct T-S balance. This excessive upwelling persistently transports the 500-1000 m fresh water over the western Pacific to the top and causes a strong negative salinity error center (the water tends to be much fresher) there. Complementary to the excessive upwelling/downwelling over the western/central Pacific Ocean, an excessive westerly undercurrent also is observed (panel *b* of Fig. 11) from the western to the central Pacific.

A multivariate assimilation scheme uses the covariance between any two variables estimated by the model ensemble to accordingly adjust the ocean state when observations of only one variable are available. Panels *c* in Figs. 5, 6, 7, 8, 10 and 11 depict the global temperature and salinity errors (top 500 m average) (Figs. 5 and 6) and the tropical temperature, salinity, vertical motion and undercurrent errors (zonal-depth sections, Fig. 7, 8, 10 and 11) when only temperature observations are assimilated but both temperature and

salinity are adjusted by applying the T-S covariance. These results are denoted by the T2TS panels. Compared to the univariate assimilation, use of the T-S covariance in the multivariate assimilation significantly improves the assimilation quality due to the maintenance of the T-S balance. Most notably, salinity errors are reduced, globally, by 44% (from panel *b* to *c* of Fig. 8), vertical motion errors by 81% (from panel *b* to *c* of Fig. 10) and the undercurrent errors by 50% (from panel *b* to *c* of Fig. 11).

We may attribute the positive T-S covariance along the thermocline (thick-red line in panel *b* of Fig. 9) to upward/downward thermocline oscillations associated with the isopycnal nature of ocean movements, and the negative T-S covariance at the top of the western Pacific to the atmospheric precipitation response associated with the warmer SST (over the ascending branch of Walker cells). It is worth mentioning that attributing the covariance to the certain physical process is usually very difficult since a covariance reflects the syntheses of the correlation between two variables over all scales of motions. From the viewpoint of *information estimation*, use of covariances is a means of trying to maintain the nature of the joint-distribution of a multivariate stochastic dynamical process, which plays an important role in solving such a complex problem as climate assessment. Previously the inconsistence of the adjusted/unadjusted temperature/salinity can only be relaxed by using a climatological T-S relationship estimated by T and S climatological data (Troccoli and Haines 1999; Han et al. 2004). More experiments with the application of covariances between temperature and currents (T-U, T-V), and zonal, meridional wind stresses (T-τ_x, T-τ_y) do not produce a dramatic improvement in the assimilation quality (not shown here) as the T-S does. However, to better maintain the nature of the joint-distribution, the long run in section 6 and follow-up studies for climate detection and/or ocean observing system evaluation all use the above-mentioned covariances associated with the ocean state.

4.2 Importance of assimilating salinity observations

With the advent of the new century, great efforts have been made to obtain more salinity measurements (Array for Real-time Geostrophic Oceanography, Argo design and deployment, for instance). The second set of experiments discussed below primarily attempts to quantify the importance of explicily assimilating observed oceanic salinity as well as temperature.

Assuming that the observational network used in section 4.1 provides both temperature and salinity measurements, the salinity profiles have the same structure as temperature profiles except that the 'observed' data is the samples (projection) of the salinity of the truth on(onto) the ocean observational network. White noise is superimposed on the projection of the model-simulated observed salinity data by the procedure described in section 3.2. Again, to maintain the nature of the joint-distribution, while assimilating the salinity, the multivariate scheme also applies the T-S covariance to adjust the temperature (denoted by TS2TS). The resulting assimilation errors are shown in panels *d* of Figs. 5, 6, 7, 8, 10 and 11 for global temperature and salinity (top 500 m average) (Figs. 5 and 6) and the tropical temperature, salinity, vertical motions and undercurrents (zonal-depth sections, Fig. 7, 8, 10 and 11). Comparing panels *d* (TS2TS case) to panels *c* (T2TS case) in the above figures, it is observed that assimilating the salinity measurements significantly improves the analysis of salinity but has a marginal effect on temperature assimilation errors. For example, salinity assimilation errors are reduced by 42% for global average (from panels *c* to *d* of Fig. 6), and 54% for the tropics (from panels *c* to *d* of Fig. 8) whereas temperature assimilation errors are reduced by only 6% for the global average (from panels *c* to *d* of Fig. 5) and 13% for the tropics (from panels *c* to *d* of Fig. 7). Again, assimilating salinity observations further improves the estimate of the joint PDF of the multivariate stochastic process, and hence the errors of both the vertical motion and the undercurrent are further reduced by approximately 13% by the introduction of salinity data (see panels *c* to *d* of Figs. 10 and 11).

The meridional heat/salt transport integrated zonally and vertically ($\int\int \rho c_p T v dx dz / \int\int \rho S v dx dz$) is an indicator of how well the ocean general circulation is estimated. Figure 12 shows the

annual mean of the integral of the meridional heat/salt transport (panel a for heat, panel b for salt) for all three data assimilation experiments. Due to the incorrectness of density in the univariate assimilation (red in panel a, denoted by T2T) the northward heat transport gradually increasing at low latitudes from south to north (black curve in panel a, denoted by truth) is significantly trapped in the tropics. The use of the T-S covariance mostly fixes this problem (green curve in panel a, denoted by T2TS). The introduction of salinity data greatly improves the southward heat transport over the southern hemisphere subtropics (blue curve in panel a, denoted by TS2TS). On the other hand, while fixing the problem of the tropical northward salt transport trap, the use of the T-S covariance over-estimates the northward salt transport in the southern hemisphere and the southward salt transport in the middle latitudes in the northern hemisphere (green curve in panel b). Such over-estimates may come from the imperfection of the T-S covariance estimates based upon the small ensemble size (6 in this case); and then these over-estimates are relaxed through direct assimilation of the salinity observations (blue curve in panel b).

5 Tests on atmospheric data assimilation (ADA): Importance of maintaining the geostrophic balance

The correlation scales employed in the atmosphere filtering analysis are 1000 km for temperature, and 500 km for u, v. In the following test cases, one or more atmospheric variables are chosen as the observed variables to be assimilated The purpose is to understand how to assimilate the atmospheric variables for improving the estimate of the atmospheric state and the fluxes it provides to other model components in the coupled modeling system. Using the observed atmospheric data produced in section 3.3, three assimilation cases are compared and analysed: 1) case I – assimilate only atmospheric winds, 2) case II – assimilate only atmospheric temperature, and 3) case III – assimilate both winds and temperature. The verification discussed below is based on the first month atmospheric data assimilation results from daily analyses.

5.1 Assimilating winds only (case I) vs. assimilating temperature only (case II)

The first experiment assimilates only winds (both u- and v-components) to adjust the atmospheric wind itself and temperature. Figure 13 presents the vertically-averaged zonal wind errors for the control case (without any data constraint) (panel a), an ODA-only case (T2TS, panel b) and the case in which based on ODA the atmospheric u and v wind components are assimilated into the atmospheric state [called ODA+ADA (wind only), panel c]. Figure 13 shows that the assimilation of u, v retrieves the true winds very well, reducing the RMS errors arround 60% from the ODA-only (comparing panel b to panel c). Figure 14 shows that reconstructing the atmospheric temperature by assimilating only temperature turns out to be somewhat more difficult than reconstructing the atmospheric winds by assimilating winds, the temperature RMS error reduction from the ODA-only being 46% (comparing panel b to panel c). Due to the improvement on the atmospheric bottom boundary conditions on SST generated by the ODA process, the ODA reduces the RMS errors for both atmospheric winds (17%, panel b of Fig. 13) and atmospheric temperature (19%, panel b of Fig. 14) compared to the control (panel a of Fig. 13 for winds and panel a of Fig. 14 for temperature).

In order to illustrate the impact of assimilating only atmospheric winds or assimilating only atmospheric temperature on the atmosphere analysis, the RMS error variation with respect to latitudes, of winds and temperature, (summed up in the zonal and vertical domain) are plotted in Fig. 15. From Fig. 15 it is observed that while the atmospheric winds are reconstructed well consistently in all latitudes by assimilating the wind observations in case I (red curve in panel a), the atmospheric temperature is improved in the tropics but becomes worse at middle and high latitudes (red curve in panel b). On the other hand, it is relatively easier to improve the estimate of winds at high latitudes than tropics by assimilating the atmospheric temperature observations in case II (green curve in panel a) while the estimate of temperature is improved in a global domain (green curve in panel b). This phenomenon

can be explained by the geostraphic balance constraint on atmospheric flows at different latitudes. In the tropics, due to the weak geostraphic balance constraint it is the winds that govern the formation of the flows in which the temperature adapts to the flow, so that once winds are corrected the temperature gets improved (case I) while the better temperature estimates do not guarantee improved winds (case II). Meanwhile at middle and high latitudes where geostraphic balance dominates the atmospheric flows, the thermal winds govern the formation of the flows so that in case I the imbalance of winds and temperature causes the temperature errors to exceed ones of the ODA-only even though the winds are corrected well, and a corrected temperature easily improves the estimate of winds in case II. These results are consistent with the simulation experiment study of Gordon et al. (1972).

Owing to the strong internal variability of the atmospheric flows and the small ensemble size in the filter (6 in this case), the use of cross-covariances between temperature and winds relaxes the imbalance only slightly, but not enough to significantly improve the assimilation quality.

5.2 Case III: Assimilating both winds and temperature

From the analyses and discussion of the last section, assimilating both the atmospheric temperature and wind observations is critically important for obtaining a self-consistent atmospheric state. In this section, we show the results of an experiment in which both winds and temperature data are assimilated. Figure 16 presents the errors of the vertical velocity in the tropics (averaged over 20^oS-20^oN) for the control (panel a) and the ODA-only (panel b) and the ODA+ADA (panel c). Figure 16 shows that since both the winds and the temperature are consistently estimated by the assimilation, the ADA (panel c) sigificantly improves the estimate of the Walker circulation in the tropics compared to the ODA-only (panel b). Nevertheless it is also clear that the estimate of the Walker circulation in the ODA-only is much better than the control. Again, this is because the ODA process provides a better SST bottom boundary condition for the atmosphere. Figure 17 depicts the errors

of the zonal wind stress that the atmosphere exerts on the ocean surface. It shows that the estimate of the zonal wind stress is improved by the ADA over much of the globe, but especially over the North Atlantic.

It's worth mentioning that although the problem discovered in the last section by assimilating monthly mean winds or temperature individually may more or less be relaxed by assimilating daily data, the destruction of the geostrophic balance while only using the atmospheric wind data is a non-negligible issue. A coherent initial condition for a reliable coupled system shall be a key element for improving the seasonal-interannual forecasts (an El Nino and Southern Oscillation, ENSO event, for instance).

6 A 25-year ODA long run test using the CDA system

The temperature of the GFDL's IPCC 20th century historical run is sampled onto the 20th century last quarter ocean temperature network (Fig. 4) to produce a 25-year idealized observed dataset, as described in section 3.2. Using the ensemble initial condition and the assimilation model configuration described in section 3.2, and the ocean assimilation parameters described in section 4.1, the assimilation system is run to assimilate the 25-year ocean temperature observations. However to simulate the sparseness of XBT observations in the deep ocean, the observations used in this experiment are limited above 500 m. Besides the temperature correction, the observed temperature is allowed to correct salinity and currents using the covariance between these variables and the temperature. And also, ocean temperature observations above 50 m are allowed to impact the zonal and meridional wind stresses (τ_x and τ_y) too, as the direct means of applying coupling dynamics into the CDA system mentioned in the introduction. The heat/water fluxes appear to be very sensitive to the adjustment by the ocean temperature observations, and due to the small ensemble size (6) used in this study, the adjustment of heat/water fluxes by the ocean temperature observations is not included here.

The error reduction of the ocean temperature over top 500 m by the ODA is presented

in Fig. 18. It is shown that the global RMS error is reduced by roughly 60% (from 0.85^{o}C to 0.35^{o}C) (panel a) during the 5-year spinup period. The 20-year time mean errors (from 1981 to 2000) of the vertically-averaged top 500 m ocean temperature are shown in panels b (control) and c (ODA). Comparing panel c to panel b, it is observed that except for the Southern Ocean (the south of 32^{o}S) and the North Atlantic, the ODA significantly reduced the temperature errors below 0.2^o from 1^o of the control. The interesting portions of the assimilation temperature errors include the southwest-northeast error belt along the northwest coast line of the Atlantic and a nearly equator-symmetric error distribution over central-east tropical Pacific. The former must be associated with the complex heat/salt transport mechanism over the North Atlantic including meridional overturning circulation (MOC) and the latter may be created by the extra Kelvin waves induced by the imbalance in the data constraint process and their reflection at the east coast. Some degree imbalance still exists in the data constraint process mainly because of an imperfect T-S relation due to the small ensemble size. On the other hand, the tempertaure assimilation errors over the Southern Ocean basically can be attributed to sparseness of observations over there (see Fig. 4).

In order to examine the capability of the ODA to reconstruct ENSO variability, the anomalies of the regionally-averaged ocean temperature over Nino3.4 are computed and presented in Fig. 19. Figure 19 shows that except for some small scale details, the ODA (2nd panel from the top, denoted by ASSIM) captures nearly all events, i.e. reproducing the phase and amplitude of all ENSO events of the truth (third panel) while the control (top, denoted by CTL) exhibits its own ENSO variability that is entirely different from the truth. The ability of the ODA to accurately reconstruct the ENSO variability can be more clearly demonstrated by the vertical average of the Nino3.4 ocean temperature anomalies (bottom panel). Note that the assimilation curve (red) follows the truth (black) very well.

Another interesting point about the coupled ODA process we want to show here is the response of the atmospheric bottom winds to the SST generated by the ODA. Figure 20 presents the zonal wind stress (τ_x) exerted on the ocean surface in the tropics by the at-

mosphere in three cases: the control (top panel), the ODA (2nd panel from the top) and the truth (third panel). First, the control τ_x shows an entirely different variability from the truth, i.e., while a few strong windbursts associated with strong ENSO events appear in the truth during the first 20 years, the control only has some weak τ_x anomalies with different phase. The ODA τ_x captures the major windburst events that occur in the truth, although the former tends to be a smoothed version of the truth. Also note that the very strong windburst event in 82/83 is reconstructed precisely.

It is useful to estimate the uncertainty of various variables of the assimilation product in an ensemble filtering framework. This exercise may further our understanding of assimilation results and possibly provides clues onto how to improve the assimilation system. The upper/lower bounds of the ODA ensemble spread of the Nino3.4 temperature anomaly averaged over top 250 m is plotted by pink-dashed lines in the bottom panel of Fig. 19. Comparing the ODA spread to the control spread (green-dashed), that is estimated by using 6 25-year non-overlap timeseries of model simulation, the ODA reduces the uncertainty of the model heat content dramatically due to the direct constraint of ocean temperature observations. However comparing the spread of assimilation wind stress (pink-dashed lines in the bottom panel of Fig. 20) to the spread of the control wind stress (green-dashed), although the entire ensemble of the ODA wind stresses appears to follow the truth's trend, the uncertainty of the zonal wind stress is only slightly reduced by the ODA. The horizontal distribution of the time mean (25 years) of standard deviations of the spread of the zonal wind stress and SST is shown in Fig. 21. The largest uncertainty of the model wind stress is located over the North Atlantic, which may be associated with the North Atlantic oscillation (NAO) phenomenon and the low-level jets there. Two other places exhibiting large model wind stress spread are the North Pacific and the high latitudes in the Southern Ocean, basically consistent with the corresponding regional storm tracks. The largest model spreads of SST (panels c) are located over the equatorial Pacific and the North Atlantic. The former reflects the ENSO variability that is associated with the Kelvin-wave activity and strong atmosphere-ocean interaction while the latter can be linked to the North Atlantic gyre. Also, some stronger spread cen-

ters associated with Rossiby-wave activity are found in the middle and high latitudes of the Pacific. Beneath the mixed layer, these Rossby-wave-related spread centers become even stronger and appear to spread over the whole Pacific (not shown here). Through the ODA, the uncertainties of ocean temperature over the Pacific and Atlantic are significantly reduced (panel *d*) by the direct assimilation of observed ocean temperatures while the uncertainties of wind stresses are reduced slightly at the equator and remain nearly unchanged off equator (panel *b*, and see the bottom of Fig. 20). In this perfect model ODA experiment, the atmospheric spread is based on both stochastic initial conditions and SST uncertainties. The difference between the wind stress spread and the ocean temperature spread generated by the ODA (in Figs. 19, 20 and 21) imply that the atmospheric spread is dominated by the strong internal variability of the atmosphere, while the convergence of SST brought about by the ODA is not sufficient to constrain the atmosphere.

Finally, timeseries of heat content anomalies in various ocean basins (basin-averaged over the top 500 m) are presented in Fig. 22. For comparison, all anomalies are computed using the truth's climatology. The ocean mask used here is the same as in the work of Levitus et al. (2000). Comparing the black curve (the truth) in Fig. 22 to the estimate of Levitus et al. (2000, Fig. 1) for the top 300 m using real ocean temperature observations, it is found that the GFDL's model simulation using the historical GHGNA radiative forcing shows a consistent multi-decadal warming trend in almost all oceans with its own inter-annual variability. Fig. 22 shows that for oceans that have reasonable observation coverage (as shown in Fig. 4) the ODA process retrieves the trend and the variability of heat content quite well, with a reduced uncertainty (pink-dashed/green-dashed curves represent the upper and lower bounds of the ODA/control spread). While the heat content anomalies of those oceans (that have a good data coverage) approch the truth quickly (i.e. within a couple of years) (e.g. over the Pacific and North Atlantic OOceans) a relatively longer spinup is required for the oceans in which data coverage is sparse (e.g. over the South Atlantic, South Indian and North Indian Oceans). It is interesting to notice that the ODA's heat content in the Southern Ocean and the Arctic Ocean follows the general trend of the truth with different

details. For example, in the assimilation, the Southern Ocean heat content remains a nearly constant departure from the truth while the Arctic Ocean heat content exhibits some strong warmer events in the middle of 1990's. Due to the lack of observations in the Southern Ocean and the Arctic Ocean (see Fig. 4), the adjustment of the trend in both oceans may be attributed to the communication between ocean circulations in different areas or/and between different coupling components (e.g. AchutaRao et al. 2006). For example, the adjustment of the Southern Ocean heat content trend can be maintained by the interaction between the circulations in the Southern Ocean and other neigbouring oceans such as the South Pacific, the South Atlantic and the South Indian Oceans, where the strong data constraint in ODA significantly corrects their circulations. The adjustment of the Arctic Ocean heat content trend may be more complex by also being associated with the ice-water interaction and ice-atmosphere flux exchanges. More detailed analyses on interactions between different ocean circulations and different coupling components and their impact on climate detection will be investigated in future studies.

7 Conclusions and discussion

We have described a coupled data assimilation (CDA) system based on the GFDL's coupled climate model (CM2) and an ensemble adjustment Kalman filter. The method produces ensemble estimates of the coupled system state and its uncertainty, by assimilating observations in a temporally-continuous manner. The resulting ensemble can then be used to initialize seasonal to multi-decadal forecasts of climate variability and trends. The experiments herein serve as a proof-of-concept ensemble data assimilation in comprehensive coupled models.

The CDA system is evaluated using a series of twin experiments, in which a particular model integration [with temporally-evolving greenhouse gases and natural aerosol (GHGNA) radiative forcings] serves as the "truth" from which observations are drawn. These experiments highlight the importance of maintaining temperature-salinity relationships (associated with particular water masses) in ocean data assimilation (ODA), and of maintaining

geostrophic balance for atmospheric data assimilation (ADA). They also address whether the ODA in the CDA system is capable of reconstructing the 20th-century variability and trends of global ocean heat content, given the 20th-century ocean observing network.

Since the atmosphere exhibits strong internal variability, a small ensemble (6 in this case) may not accurately evaluate the covariance among the simulated fields – and thus the assimilation cannot effectively adjust the analysis solution away from the observational locations. The ADA experiments with dense atmospheric observations suggest that in the tropics, observations of the winds are most useful in reconstructing the atmospheric state (Gordon et al. 1972); while in mid- and high-latitudes, atmospheric temperature are more useful for establishing geostrophic balance. The more slowly-evolving ocean, in contrast, appears amenable to assimilation even with the samll ensemble. The ODA effectively utilizes the T-S covariances to maintain realistic water masses, isopycnal transports, and the observed co-location of warm SST and enhanced precipitation in tropical warm pool regions, even when temperature-only observations are assimilated. At higher latitudes, direct salinity observations become more important for constraining the ocean circulation.

To test how well the analysis system reconstructs the oceanic impacts of 20th-century radiative forcing changes, we performed a 25-year CDA using the historical oceanic temperature observing network. We find that the assimilation takes at most five years to spin up to equilibrium, at which point the heat content in all eight ocean basins closely resembles the true trends and variability – with a 60% reduction in RMS ocean temperature errors relative to an unconstrained control run. The true heat content variability is captured best in the Pacific, where the data coverage is relatively dense; ENSO variations in particular are reconstructed very well. The analysis less skillful in high-latitude regions, where observations are extremely sparse over the 20th century; while the assimilation is unable to capture the interannual variability of oceanic heat content, it does reconstruct the long-term trend teleconnected from lower latitudes.

The purpose of this study has been to outline the design, implementation, and initial

evaluation of the ensemble CDA system, in terms of reconstructing the 20th-century oceanic temperature trends and variability. In a series of follow-up studies, we intend to explore several remaining issues:

1. Impacts of temporally-varying radiative forcing on the state estimate. The present study represents a particularly stringent test for the CDA, in that the "truth" run feels historically-evolving GHGNA forcings, while the assimilation run feels GHGNA radiative forcings from a fixed year (1860). Presumably more realistic radiative forcing will improve the CDA performance.

2. Impacts of the observational network on the detection of climate variability and trends. In particular, we will explore to what extent the deep-profile temperature and salinity measurements from Argo floats can better constrain the assimilation in high latitudes, which experience substabtial freshwater input from river runoff and melting ice. These freshwater inputs, combined with strong thermohaline transports, may be a key in determining the Atlantic meridional overturning circulation (MOC) – an important source of multi-decadal climate variability and trends.

3. Impacts of atmospheric observations on the coupled state estimate, and on the initial conditions used for forecasts of global climate. Presumably this will have a positive impact for the tropics and ENSO, where the air-sea fluxes of heat and momentum are largely controlled by the atmosphere. Estimation and prediction of the high latitude oceans and the global ocean circulation may also benefit from ADA, given the link between atmospheric NAO and the MOC (Delworth and Greatbatch 2000; Delworth and Dixon 2000).

4. Impacts of model drifts and biases on the assimilation skill. Mainly, two approaches we would like to explore include: (a) assimilation of additional kinds of observations – such as satellite SSTs and altimeter (Mellor and Ezer, 1991), and ocean currents from drifting and moored buoys for increasing the sample size of oceanic observations; and (b) the use of multiple coupled models and multiple model parameters in the assimilating ensemble for improving the estimate of the prior PDF. In particular, for the first approach, since altimeter

data contain the temperature and salinity information within the whole water column, based on the model dynamics the ensemble filter may project sea surface height information onto the vertical structure so as to correct the biases underneath the surface. Therefore, once real data assimilation is initialized, use of altimeter data in assimilation and evaluation of their impact on assimilation quality shall be ranked as a leading order priority. The second approach not only benefits the assimilation by improving the prior PDF estimate but also enhances the probablistic forecast quality by initializing the multiple model ensemble forecasts.

ACKNOWEDGEMENT

Thanks to Dr. J. L. Anderson for generous discussions on the early parallel design of the ensemble system, and to V. Balaji for his continuing support of the parallel code and environment. Thanks to Dr. Guijun Han for her suggestions in processing observation data during her visit at GFDL. Thanks also to F. Zeng, Mike Spelman, Z. Liang and H. Lee for their helps in configuring the coupled model; F. Zeng also provided frequent help with data processing and visualization. The authors thank Drs. T. Gordon, S. Fan and H. Lee, for their comments on earlier versions of this manuscript.

REFERENCES

AchitaRao, K. M., B. D. Santer, P. J. Gleckler, K. E. Taylor, D. W. Pierce, T. P. arnett, and T. M. L. Wigley, 2006: Variability of ocean heat uptake: Reconciling observations and models. *J. Geophys. Res.*, **111(C0)**, 5019, doi:10.1029/2005JC003136.

Troccoli, A. and K. Haines, 1999: Use of the temperature-salinity relation in a data assimilation context. *Journal of Atmospheric and Oceanic Technology*, **Vol. 16, No. 12**, 2011–2025.

Anderson, J. L., 2003: A local least squares framework for ensemble filtering. *Mon. Wea. Rev.,* **131**, 634–642.

Anderson, J. L., 2001: An ensemble adjustment Kalman filter for data assimilation. *Mon. Wea. Rev.,* **129**, 2884–2903.

Bishop, C. H., B. J. Etherton and S. Majumdar, 2001: Adaptive sampling with the ensemble transform Kalman filter, part I. *Mon. Wea. Rev.,* **129**, 420–436.

Delworth, T. L., A. J. Broccoli, A. Rosati, R. J. S. V. Balaji, J. A. Beesley, W. F. Cooke, K. W. Dixon, J. Dunne, K. A. Dunne, J. W. Durachta, K. L. Findell, P. Ginoux, A. Gnanadesikan, C. T. Gordon, S. M. Griffies, R. Gudgel, M. J. Harrison, I. M. Held, R. S. Hemler, L. W. Horowitz, S. A. Klein, T. R. Knutson, P. J. Kushner, A. L. Langenhorst, H.-C. Lee, S. J. Lin, J. Lu, S. L. Malyshev, P. C. Milly, V. Ramaswaami, J. Russell, M. D. Schwarzkopf, E. Shevliakova, J. Sirutis, M. Spelman, W. F. Stern, M. Winton, A. T. Wittenberg, B. Wyman, F. Zeng, and R. Zhang, 2005: GFDL's CM2 global coupled climate models, Part I: Fornulation and simulation characteristics. *J. Climate*, **in press**.

Evensen, G., 1994: Sequential data assimilation with a nonlinear quasi-geostrophic model using Monte Carlo methods to forecast error statistics. *J. Geophys. Res.*, **99**, 10143–10162.

Fedorov, A. V. and S. G. Philander, 2001: Is El Niño changing? *Science*, **288**, 1997–2001.

GFDL Global Atmospheric Model Development Team, 2004: The new GFDL global at-

mosphere and land model AM2/LM2: Evaluation with prescribed SST simulations. *J. Climate.*, **17**, 4641–4673.

Gnanadesikan, A., K. W. Dixon, S. M. Griffies, V. Balaji, J. A. Beesley, W. F. Cooke, T. L. Delworth, M. J. Harrison, I. M. Held, W. J. Hurlin, H.-C. Lee, Z. Liang, G. Nong, R. C. Pacanowski, A. Rosati, J. Russell, B. L. Samuels, S. M. Song, M. J. Spelman, R. J. Stouffer, C. O. Sweeney, G. Vacchi, M. Winton, A. T. Wittenberg, R. Zhang and F. Zeng, 2005: GFDL's CM2 global coupled climate models, Part II: The baseline ocean simulation. *J. Climate.*, **19**, 675–697.

Gordon, C. T., L. Umscheid, Jr., and K. Miyakoda, 1972: Simulation experiments for determining wind data requirements in the tropics. *J. Atmos. Sci.,* **29**, 1064–1075.

Griffies, S. M., et al., 2005: Formulation of an ocean model for a coupled climate simulation, **in press**, *Ocean Modeling.*

Griffies, S. M., M. J. Harrison, R. C. Pacanowski and A. Rosati, 2003: A Technical Guide to MOM4. *GFDL Ocean Group Technical Report*, No. 5, Princeton, NJ 08542, NOAA/Geophysical Fluid Dynamics Laboratory, 295 pp.

Griffies, S. M., M. J. Harrison, R. C. Pacanowski and A. Rosati, 2003: A Technical Guide to MOM4. *GFDL Ocean Group Technical Report*, No. 5, Princeton, NJ 08542, NOAA/Geophysical Fluid Dynamics Laboratory, 295 pp.

Griffies, S. M. and R. W. Hallberg, 2000: Biharmonic friction with a Smagorinsky-like viscosity for use in large-scale eddy-permitting ocean models. *Mon. Wea. Rev.,* **128**, 2935–2946.

Hamill, T. M., J. S. Whitaker and C. Snyder, 2001: Distance-dependent filtering of background error covariance estimates in an ensemble Kalman filter. *Mon. Wea. Rev.,* **129**, 2776–2790.

Han, G., J. Zhu and G. Zhou, 2004: Salinity estimation using the T-S relation in the context of variational data assimilation. *J. Geophys. Res.*, **109(C0)**, 3018, doi:10.1029/2003JC001781.

Hahn, D. G. and S. Manabe, 1982: Obserational network and climate monitoring. *In Proceedings of the Sixth Annual Climate Diagnostics Workshop, Washington, DC: U.S. Dept. of Commerce, National Oceanic and Atmospheric Administration, 229-235.*

Harrison, M. J., A. Rosati, R. Gudgel and J. Anderson, 1996: Initialization of coupled model forecasts using an improved ocean data assimilation system. *11th Conference on Numerical Weather Prediction, Boston, MA.*

Houtekamer, P. L. and H. L. Mitchell, 1998: Data assimilation using an ensemble Kalman filter technique. *Mon. Wea. Rev.,* **126**, 796–811.

Houtekamer, P. L. and H. L. Mitchell, 2001: A sequential ensemble Kalman filter for atmospheric data assimilation. *Mon. Wea. Rev.,* **129**, 123–137.

Hunke, E. C., and J. K. Dukowicz, 1997: An elastic-viscous-plastic model for sea ice dynamics, *J. Phys. Oceanogr.*, **27**, 1849–1867.

Jazwinski, A. H., 1970: *Stochastic Processes and Filtering Theory.* Academic Press, New York, 376pp.

Levitus, S. and T. P. Boyer, 1994: World ocean atlas, 1994 volume 4: Temperature. *NOAA NESDIS Atlas*, 4, U.S. Department of Commerce, Washington, D. C.

Levitus, S. and J. I. Antonov, 1997: Climatological and Interannual Variability of Temperature, Heat Storage and rate of Heat Storage in the Upper Ocean. *NOAA NESDIS Atlas*, 16, U.S. Department of Commerce, Washington, D. C.

Levitus, S., J. I. Antonov, T. P. Boyer and C. Stephens, 2000: Warming of the World Ocean. *SCIENCE*, **287**, 2225–2229.

Levitus, S., J. I. Antonov, T. P. Boyer, 2005: Warming of the World Ocean. *Geophys. Res. Lett.*, **32**, 1955–2005.

Lorenz, E. N., 1963: Deterministic non-periodic flow. *J. Atmos. Sci.,* **20**, 130–141.

Mellor, G. L. and T. Ezer, 1991: A Gulf Stream model and an altimetry assimilation scheme.

J. Geophys. Res, **96**, 8779–8795.

Miller, R. N., M. Ghil and P. Gauthiez, 1994: Advanced data assimilation in strongly nonlinear dynamical system. *J. Atmos. Sci.,* **51**, 1037–1056.

Miller, R. N., 1998: Introduction to the Kalman filter. In: *Proceedings of the ECMWF Seminar on Data Assimilation*. European Center for Medium Range Weather Forecasting, Shinfield Park, Reading, RG2 9AX UK, 9-11 September, 1996, 47–59.

Miller, R. N., E. F. Carter and S. T. Blue, 1999: Data assimilation into nonlinear stochastic models. *Tellus,* **51A**, 167–194.

Mitchell, H. L., and P. L. Houtekamer, 2000: An adaptive ensemble Kalman filter. *Mon. Wea. Rev.,* **128**, 416–433.

Rahmstorf S., 1995: Bifurcations of the Atlantic thermohaline circulation in response to changes in the hydrological cycle. *Nature*, **378**, 145–149.

Rosati, A., K. Miyakoda and R. Gudgel, 1997: The impact of ocean initial conditions on ENSO forecasting with a coupled model. *Mon. Wea. Rev.,* **125**, 754–772.

Winton, M., 2000: A reformulated three-layer sea ice model. *J. Atmos. Ocean. Tech.*, **17**, 525–531.

Whitaker, J. S., and T. M. Hamill, 2002: Ensemble data assimilation without perturbed observations. *Mon. Wea. Rev.,* **in press**.

Zhang, S. and J. L. Anderson, 2003: Impact of spatially and temporally varying estimates of error covariance on assimilation in a simple atmospheric model. *Tellus,* **55A**, 126–147.

Zhang, S., M. J. Harrison, A. T. Wittenberg, and A. Rosati, J. L. Anderson and V. Balaji, 2005: Initialization of an ENSO forecast system using a parallelized ensemble filter. *Mon. Wea. Rev.,* **133**, 3176–3201.

Zhang, S., A. Rosati and M. J. Harrison, 2006: Coupled ensemble data assimilation for global oceanic climate studies, Part II: Impact of ocean observing system on detection of

ocean heat content and salinity variability. to be submitted to *J. of Climate*

FIGURE CAPTIONS

Fig. 1 Schematic diagram illustrating how the GFDL's coupled model exchanges fluxes between model components (black arrows), and constraints of oceanic/atmospheric observations in this particular climate detection study (red arrows). The dashed green arrow denotes the radiative forcings in the coupled system, and the dashed means that the radiative forcings used during assimilation is set as fixed-year (1860).

Fig. 2 Cartoon of how a two-step data assimilation procedure works for updating the estimate of the probability distribution of a single state variable, x, given a single observation, y, in in the ensemble adjustment Kalman filter (EAKF) under the least squares framework. The righthand column represents step one: updating the probability density function (PDF) at the observation location as a new observation comes in (denoted by thick-dotted arrow STEP1). The solid arrow 1 denotes that the prior PDF at the observation location is squashed by a new observation (denoted by the right-bottom dashed curve), computed by Eq. (3), and the solid arrow 2 represents the shift of the prior ensemble mean at the observation location due to the new observation, computed by Eq. (5). The thick-dotted arrow from the righthand column to the lefthand column denotes the step two: using the correlation distribution (shaded region) to distribute the observation increments to impacted gridpoints, computed by Eq. (6). The solid arrow 3 represents the process of updating the PDF of a gridpoint.

Fig. 3 Flow-chart of the GFDL's super-parallelized coupled data assimilation system for 180 PEs case. Generally, this system can be scaled for any ensemble size and any big enough processing element (PE) number. But in practice due to efficiency consideration it is currently scaled for running 6, 12, 24 ensemble members by invoking a minimum of 120 PEs, and a maximum of 1440 PEs on the Altix (GFDL's IC cluster or NASA's Columbia cluster).

Fig. 4 Samples of ocean observational network during the last quarter of the 20th century.

Fig. 5 Annual mean ocean potential temperature errors averaged over top 500 m for 1) the control, simulation with no data constraint, b) only allowing temperature observations to impact temperature itself (denoted by T2T, univariate analysis scheme), c) allowing temperature observations to impact both temperature and salinity using their cross-covariance (denoted by T2TS, multivariate analysis scheme) and d) using both temperature and salinity observations to adjust both temperature and salinity (denoted by TS2TS, multivariate analysis scheme). The contour interval is 0.2^oC and contour 0 is omitted. The number at the upperright of each panel marks the root mean square error of the top 500 m ocean potential temperature for each case.

Fig. 6 Same as Fig. 5 except for the salinity and the contour interval is 0.05 PSU.

Fig. 7 Same as Fig. 5 except for an x-z section at the equator.

Fig. 8 Same as Fig. 7 except for salinity and the contour interval is 0.05 PSU.

Fig. 9 Annual mean corrections of potential temperature (a) and salinity (c), and the T-S covariance distributed on the x-z section at the equator produced by the T2TS analysis scheme (b). The contour interval is 0.01^oC for (a), 0.002 PSU ^{o}C for (b) and 0.005 PSU for (c).

Fig. 10 Same as Fig. 7 except for the vertical motions and the contour interval is 0.05 m/day.

Fig. 11 Same as Fig. 7 except for the undercurrent and the contour interval is 0.05 m/s.

Fig. 12 The zonal and vertical integral of the meridional heat (a) and salinity (b) transports in the truth (black), univariate assimilation (T2T, red), the multivariate assimilation using T-S covariance without salinity observations (T2TS, green) and the multivariate assimilation using both T and S observations (TS2TS, blue).

Fig. 13 The atmospheric vertically-averaged zonal wind errors for (a) the control, (b) the ODA-only and (c) the case with ODA plus the atmospheric wind assimilation. The

contour interval is 2 m/s. The contour 0 is omitted.

Fig. 14 The atmospheric vertically-averaged temperature errors for (a) the control, (b) the ODA-only (T2TS case) and (c) the case with ODA plus the atmospheric temperature assimilation. The contour interval is 0.5°C. The contour 0 is omitted.

Fig. 15 The RMS errors computed on zonal-vertical domain, for the atmospheric zonal wind (a) and the atmospheric temperature (b) in the ODA-only (black), the case with ODA plus the atmospheric wind assimilation (red) and the case with ODA plus the atmospheric temperature assimilation (green).

Fig. 16 Vertical motion errors of the tropical atmosphere (averaged over 20^oS-20^oN for the control (a), the ODA-only (b) and ODA+ADA (c). The contour interval is 0.1 m/day. The contour 0 is omitted.

Fig. 17 Zonal wind stress errors for the control (a), the ODA-only (b) and ODA+ADA (c). The contour interval is 0.04 N/m^2. The contour 0 is omitted.

Fig. 18 Timeseries of the global RMS error of the top 500 m ocean temperature (a) for the control (dotted) and the ODA (solid), and time mean of vertically-averaged ocean temperature errors over the top 500 m. The contour interval in (b) and (c) is 0.2^oC. The contour 0 is omitted.

Fig. 19 Timeseries of the anomalies of the Nino3.4 ocean temperature for the control (denoted by CTL), the ODA (denoted by ASSIM) and the truth. Curves in the bottom panel are the vertical averages over top 250 m for the control (blue), the ODA (red) and the truth (black). The upper and lower bounds of the control/ODA spread are plotted by the green-dashed/pink-dashed lines in the bottom panel. The control (model climatological) spread is estimated by 6 25-year non-overlap timeseries and the ODA spread is computed by 6 ensemble members in the filter. All anomalies are computed using the truth's climatology and the contour interval for the first three panels is 0.5^oC.

Fig. 20 Timeseries of the anomalies of the zonal wind stress (τ_x) at the tropical Pacific (5^oS-5^oN average for the control (denoted by CTL), the ODA (denoted by ASSIM) and the truth. Curves in the panel next to the bottom are the zonal averages over the Pacific for the control (green), the ODA (red) and the truth (black). The upper and lower bounds of the control/ODA spread are plotted by the green-dashed/pink-dashed lines in the bottom panel. The method for estimating the spread is the same as for Fig. 19. All anomalies are computed using the truth's climatolgy and the contour interval for the first three is 0.01 N/m^2.

Fig. 21 Time mean of the standard deviations of the zonal wind stress spread (top *a*, *b*) and the SST spread (bottom *c*, *d*) in the control (left *a*, *c*) and ODA (right *b*, *d*). The method for estimating the spread is the same as for Fig. 19. The contour interval is 0.01 N/m^2 for *a*, *b*, and 0.1^oC for *c*, *d*.

Fig. 22 Timeseries of the anomalies of the top 500 m ocean heat content (averaged temperature) in different oceans for the truth (black), the ODA (red) and the control (blue). The upper and lower bounds of the control/ODA spread are plotted by the green-dashed/pink-dashed lines. The method for estimating the spread is the same as for Fig. 19. All anomalies are computed using the truth's climotolgy.

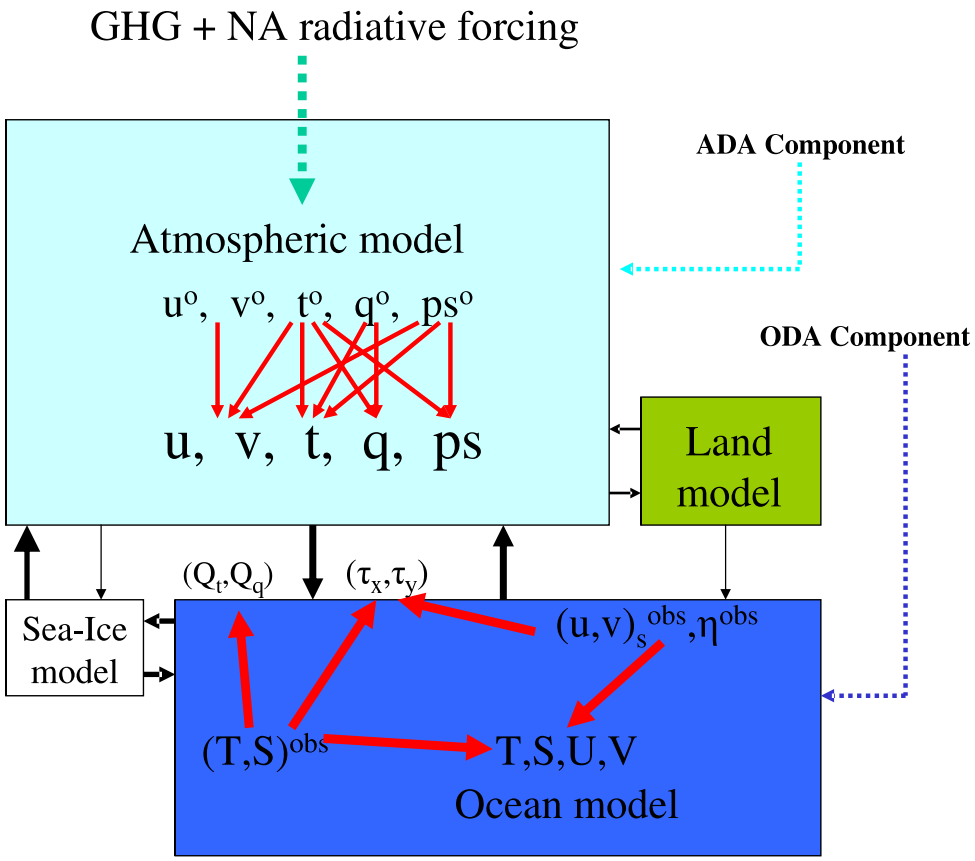

Figure 1: Schematic diagram illustrating how the GFDL's coupled model exchanges fluxes between model components (black arrows), and constraints of oceanic/atmospheric observations in this particular climate detection study (red arrows). The dashed green arrow denotes the radiative forcings in the coupled system, and the dashed means that the radiative forcings used during assimilation is set as fixed-year (1860).

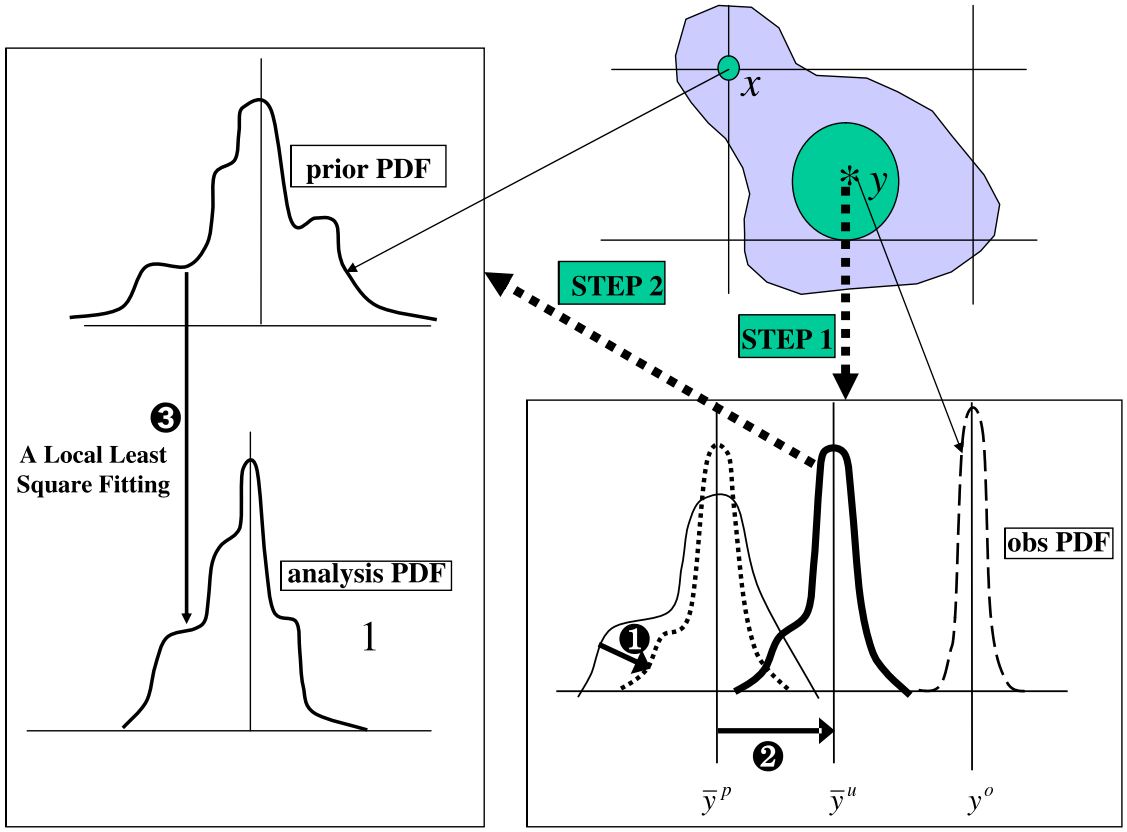

Figure 2: Cartoon of how a two-step data assimilation procedure works for updating the estimate of the probability distribution of a single state variable, x, given a single observation, y, in in the ensemble adjustment Kalman filter (EAKF) under the least squares framework. The righthand column represents step one: updating the probability density function (PDF) at the observation location as a new observation comes in (denoted by thick-dotted arrow STEP1). The solid arrow 1 denotes that the prior PDF at the observation location is squashed by a new observation (denoted by the right-bottom dashed curve), computed by Eq. (3), and the solid arrow 2 represents the shift of the prior ensemble mean at the observation location due to the new observation, computed by Eq. (5). The thick-dotted arrow from the righthand column to the lefthand column denotes the step two: using the correlation distribution (shaded region) to distribute the observation increments to impacted gridpoints, computed by Eq. (6). The solid arrow 3 represents the process of updating the PDF of a gridpoint.

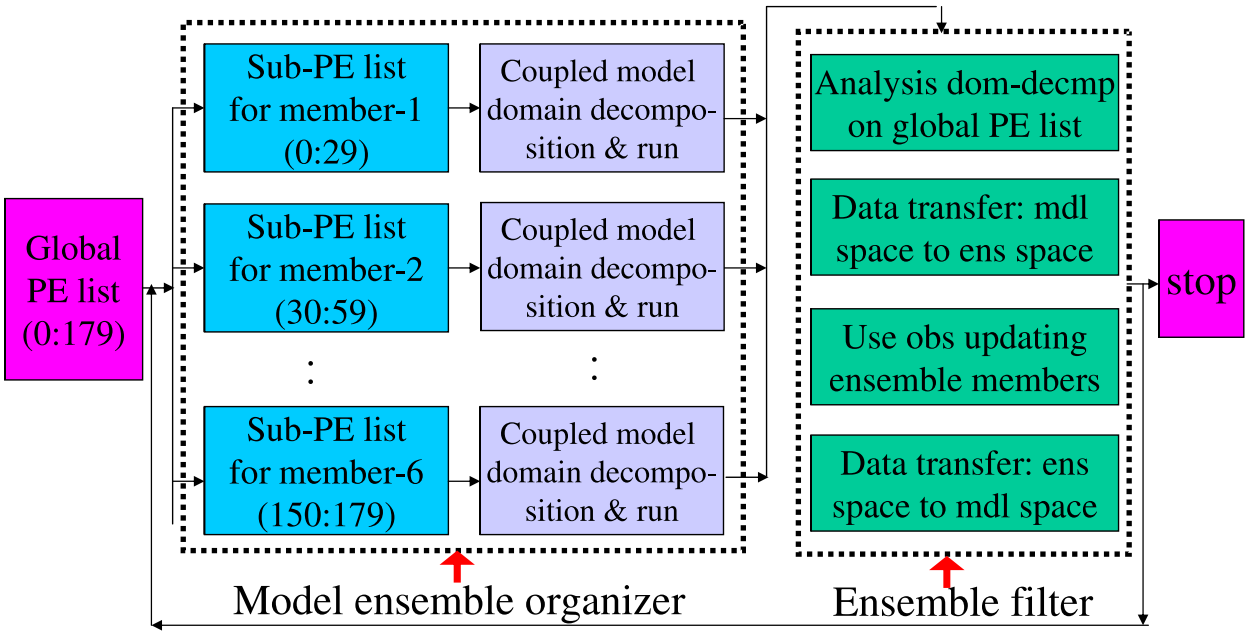

Figure 3: Flow-chart of the GFDL's super-parallelized coupled data assimilation system for 180 PEs case. Generally, this system can be scaled for any ensemble size and any big enough processing element (PE) number. But in practice due to efficiency consideration it is currently scaled for running 6, 12, 24 ensemble members by invoking a minimum of 120 PEs, and a maximum of 1440 PEs on the Altix (GFDL's IC cluster or NASA's Columbia cluster).

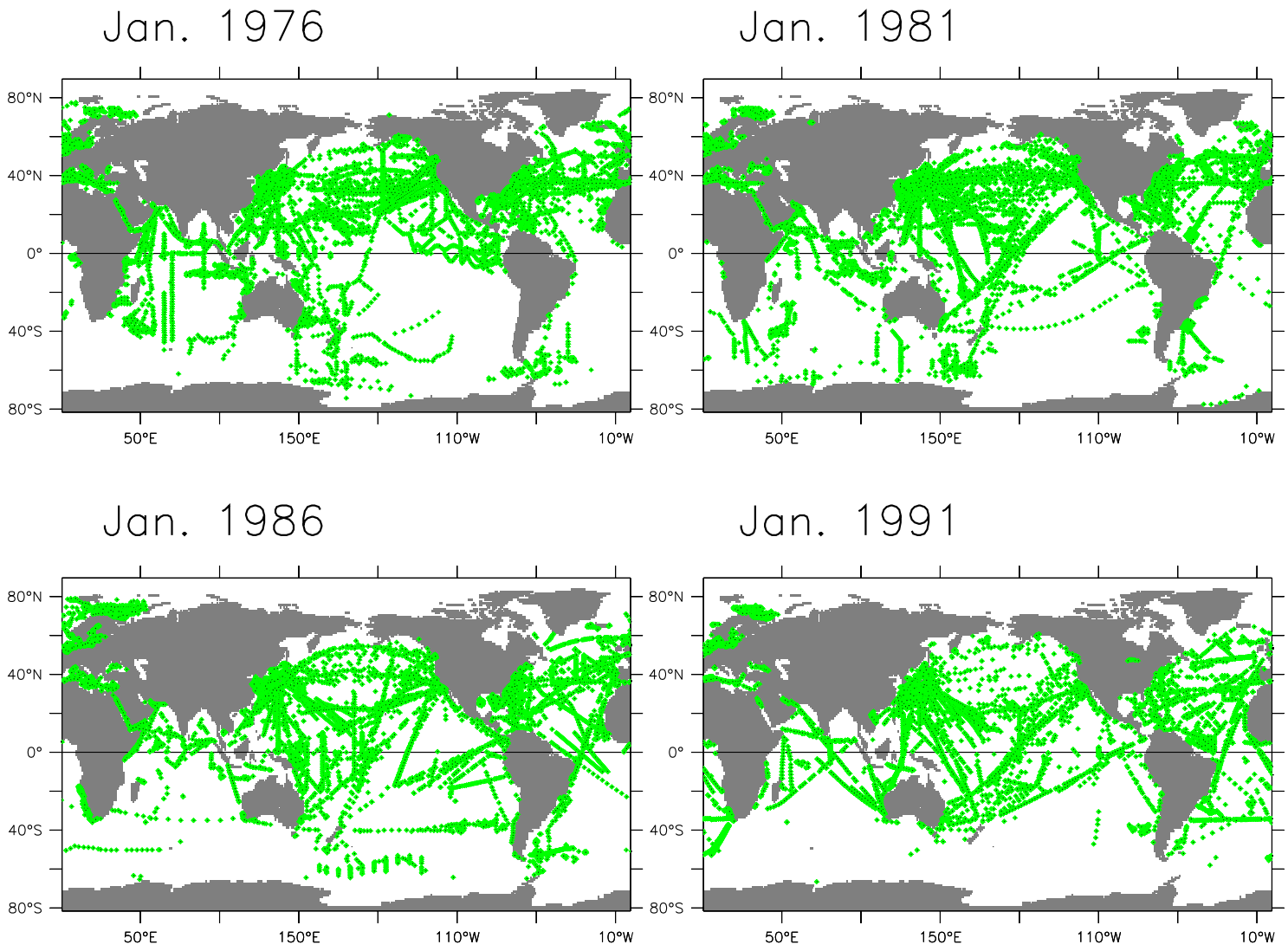

Figure 4: Samples of ocean observational network during the last quarter of the 20th century.

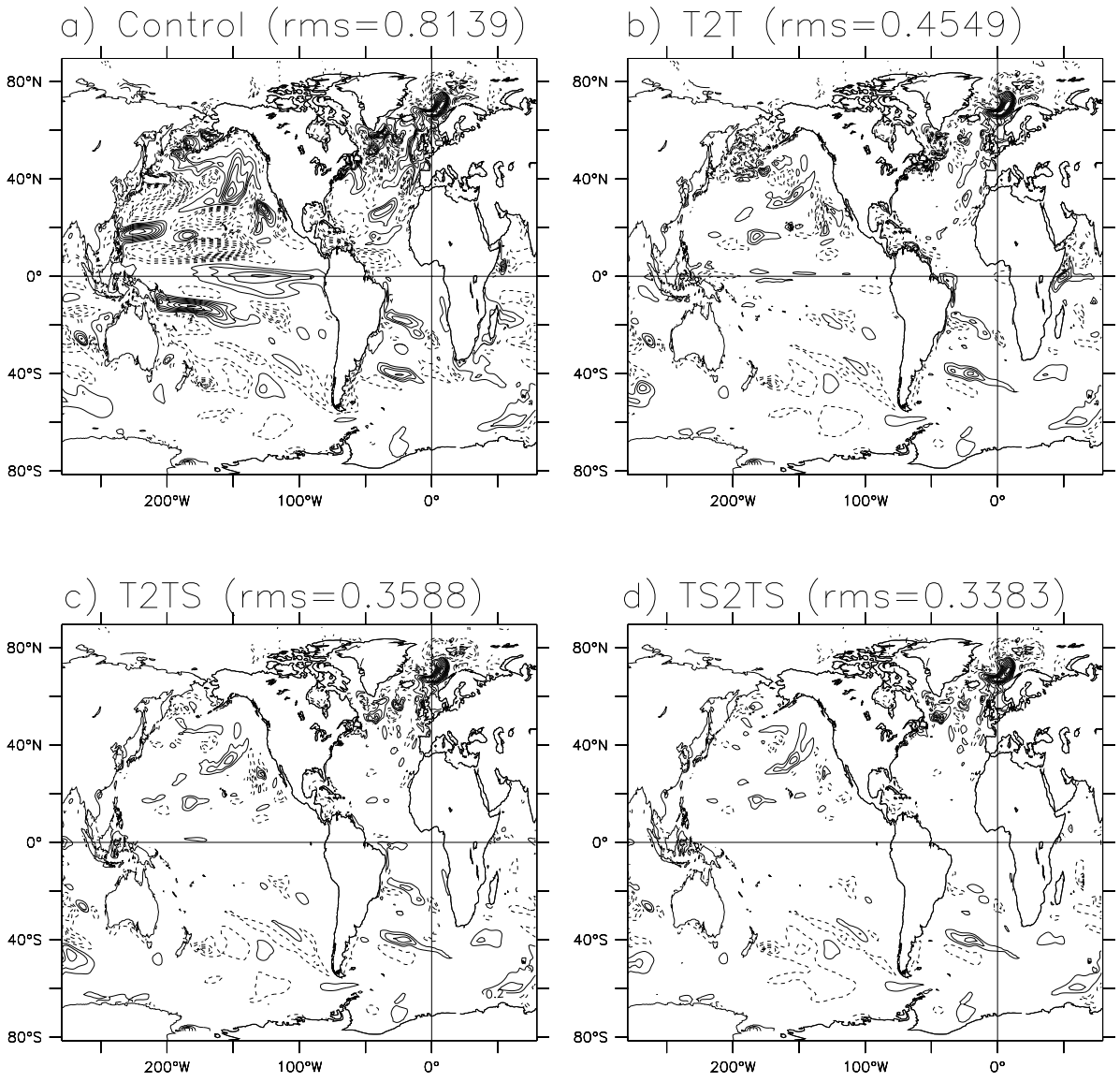

Figure 5: Annual mean ocean potential temperature errors averaged over top 500 m for 1) the control, simulation with no data constraint, b) only allowing temperature observations to impact temperature itself (denoted by T2T, univariate analysis scheme), c) allowing temperature observations to impact both temperature and salinity using their cross-covariance (denoted by T2TS, multivariate analysis scheme) and d) using both temperature and salinity observations to adjust both temperature and salinity (denoted by TS2TS, multivariate analysis scheme). The contour interval is 0.2^{o}C and contour 0 is omitted. The number at the upperright of each panel marks the root mean square error of the top 500 m ocean potential temperature for each case.

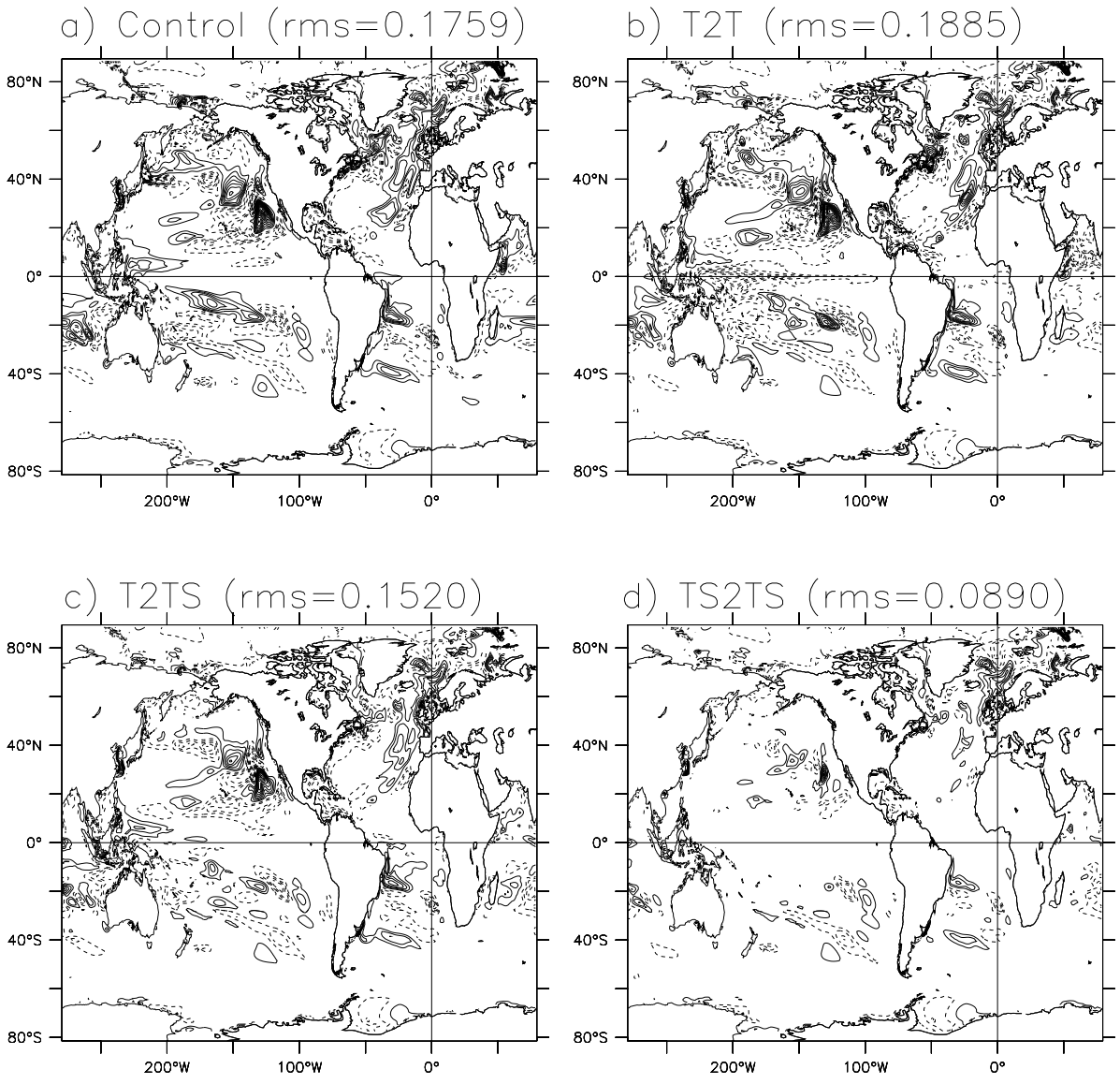

Figure 6: Same as Fig. 5 except for the salinity and the contour interval is 0.05 PSU.

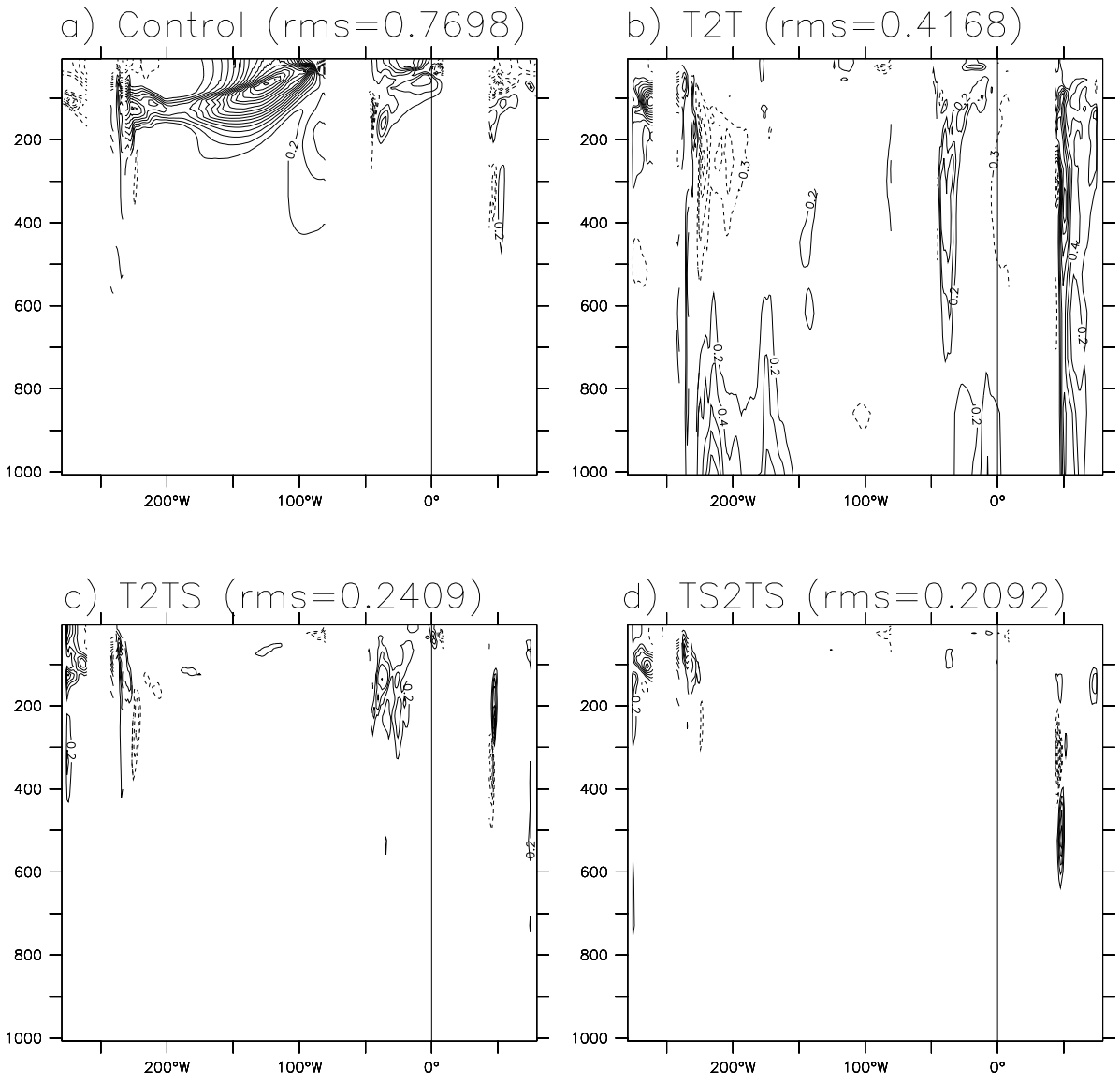

Figure 7: Same as Fig. 5 except for x-z section at the equator.

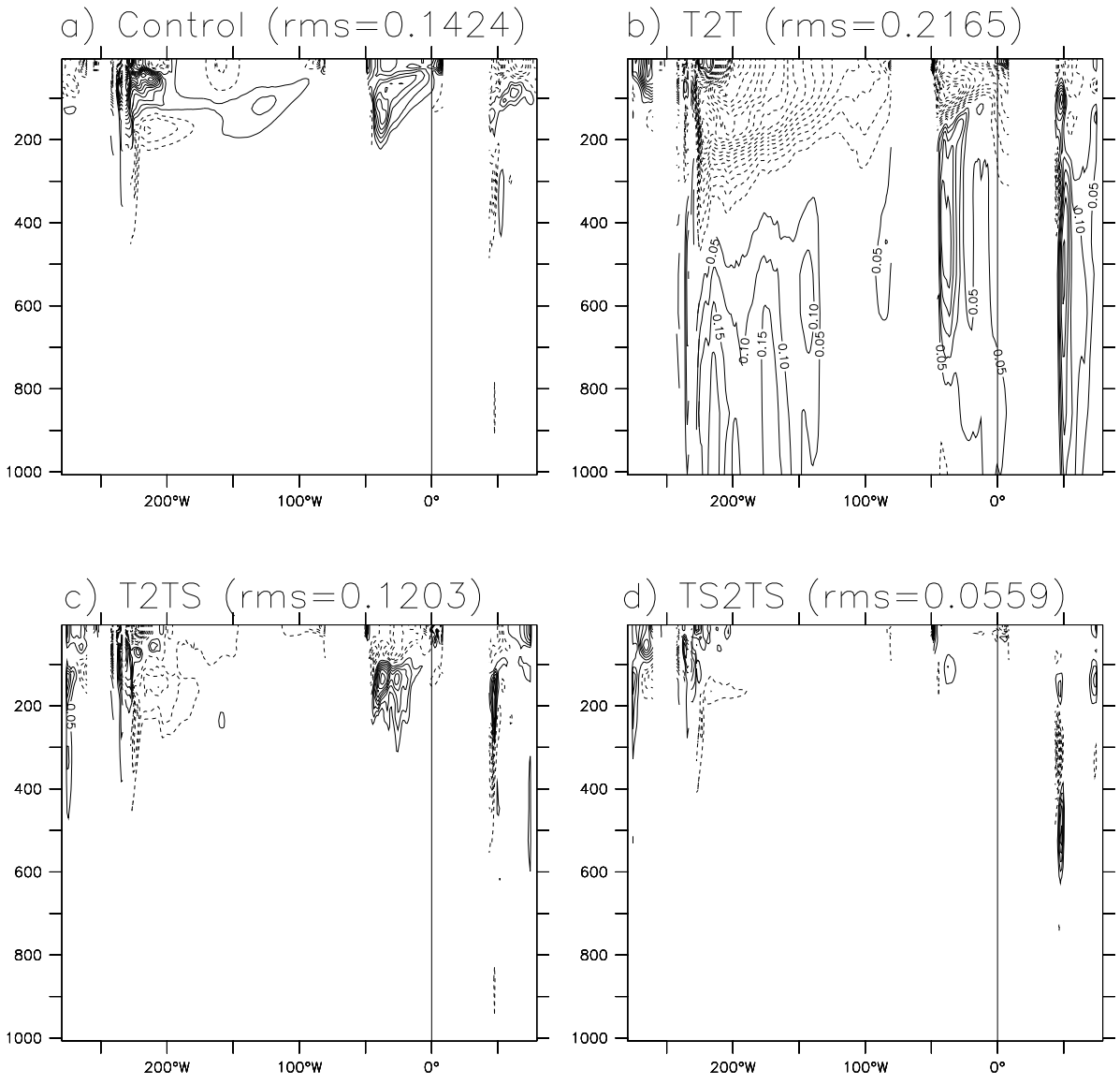

Figure 8: Same as Fig. 7 except for salinity and the contour interval is 0.05 PSU.

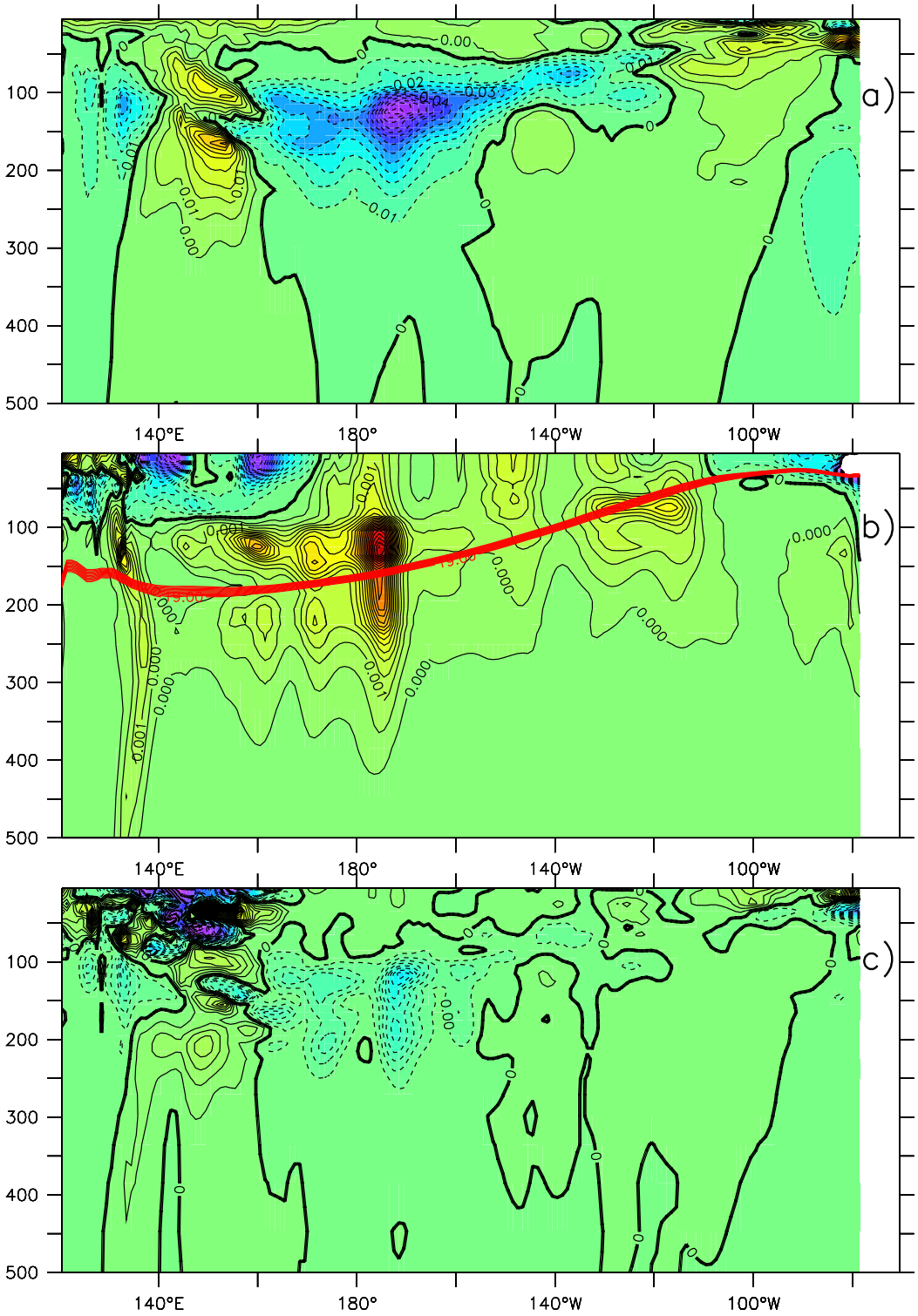

Figure 9: Annual mean corrections of potential temperature (a) and salinity (c), and the T-S covariance distributed on the x-z section at the equator produced by the T2TS analysis scheme (b). The contour interval is 0.01^{o}C for (a), 0.002 PSU ^{o}C for (b) and 0.005 PSU for (c).

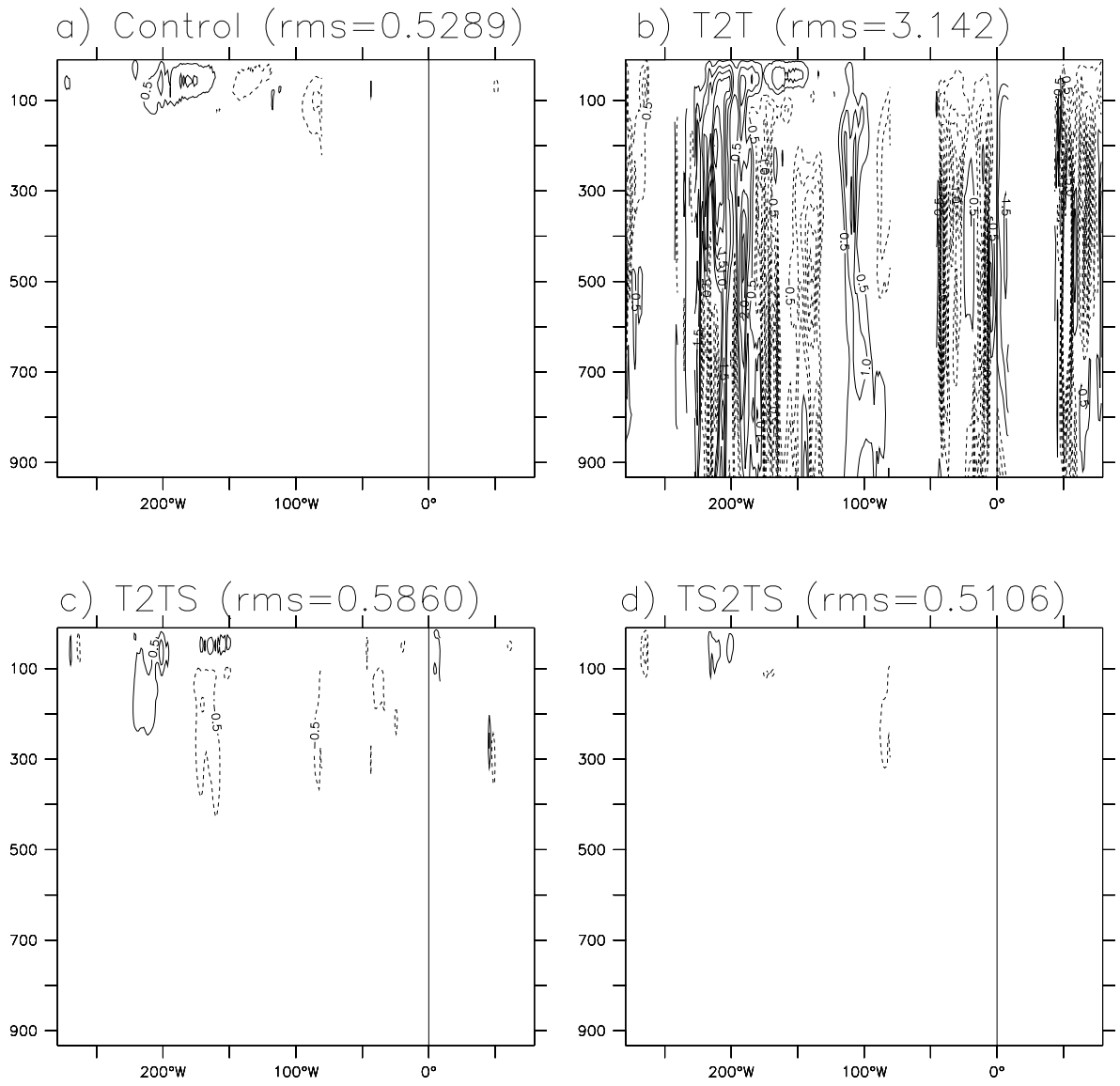

Figure 10: Same as Fig. 7 except for the vertical motions and the contour interval is 0.05 m/day.

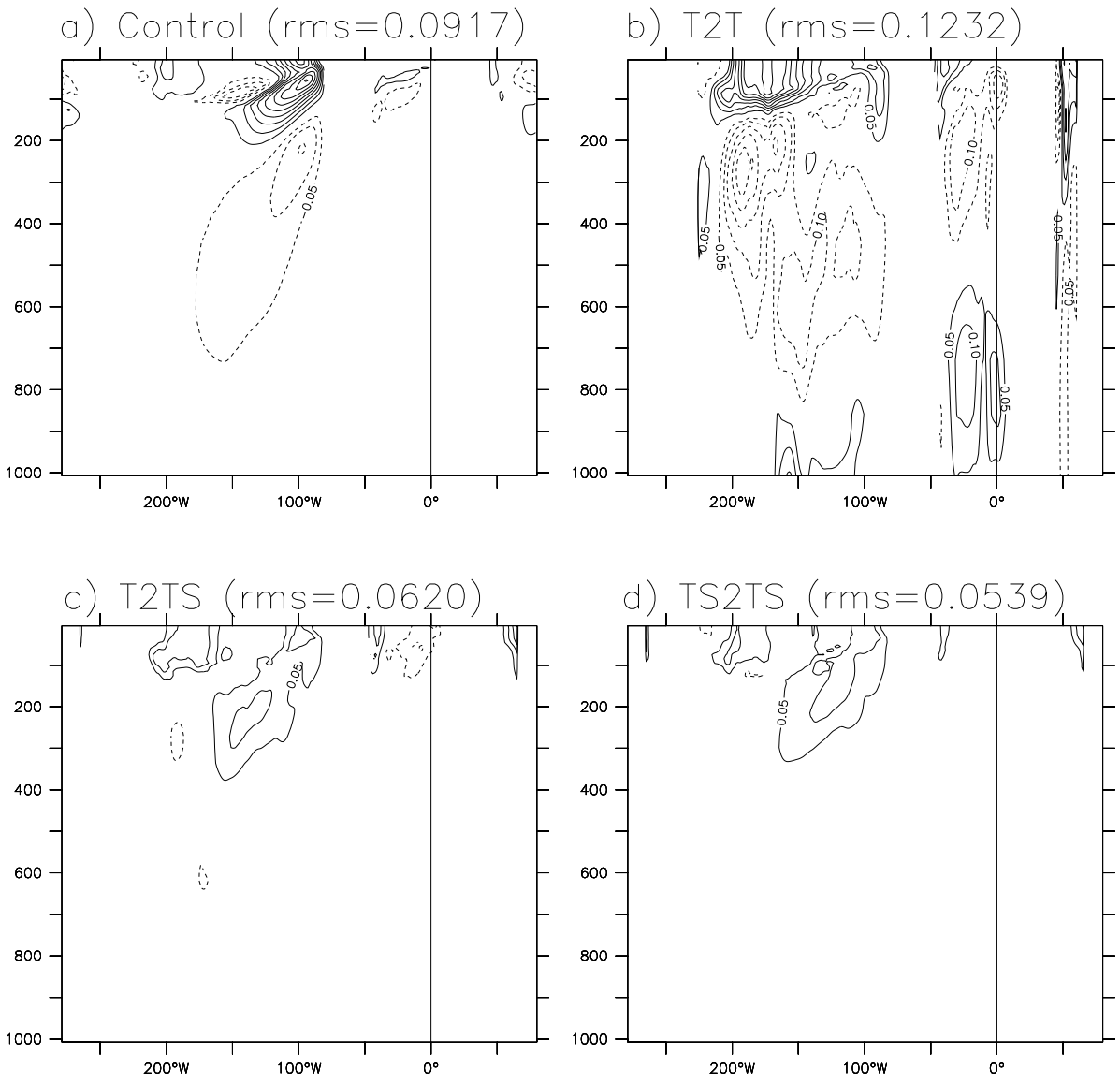

Figure 11: Same as Fig. 7 except for the undercurrent and the contour interval is 0.05 m/s.

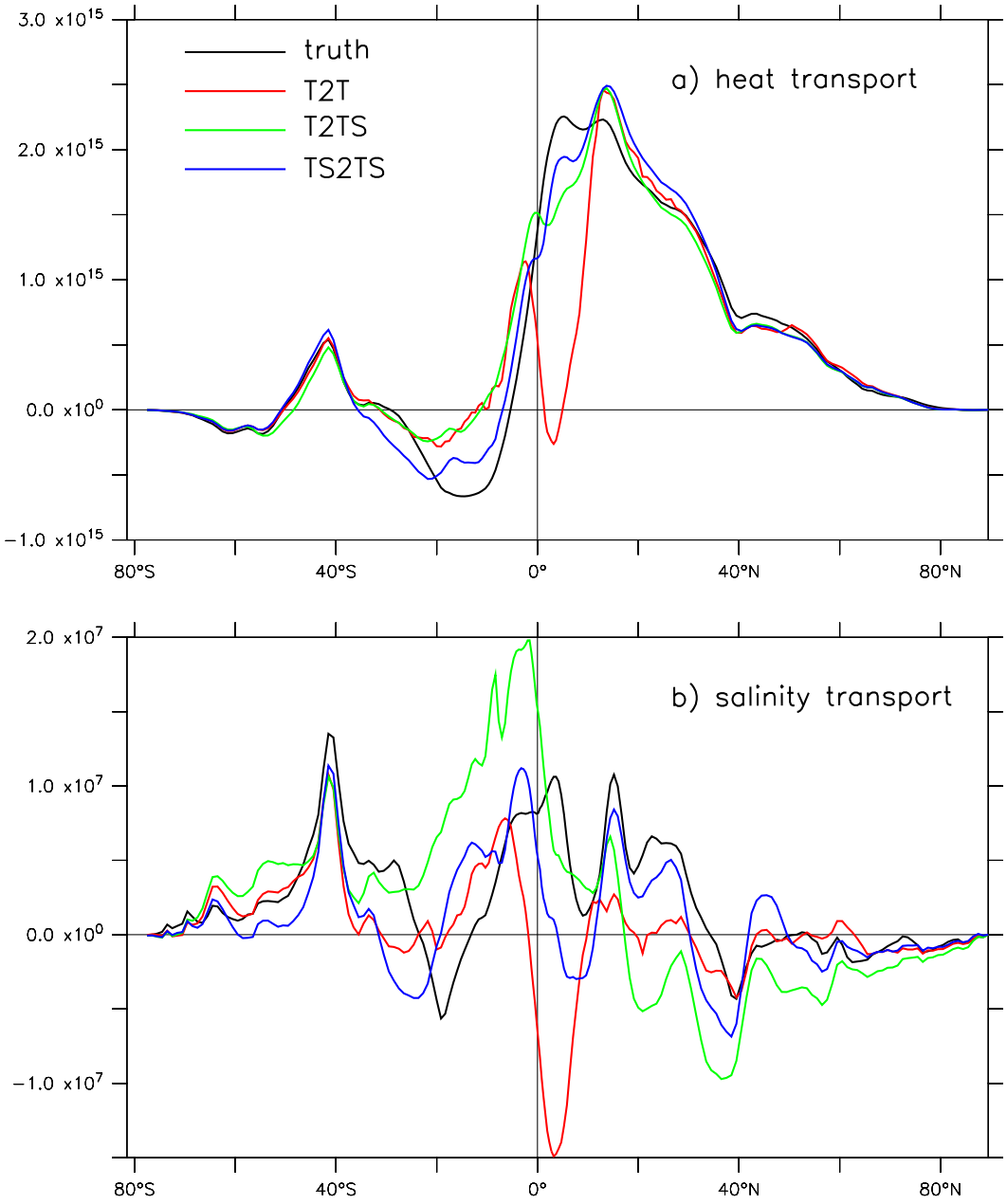

Figure 12: The zonal and vertical integral of the meridional heat (a) and salinity (b) transports in the truth (black), univariate assimilation (T2T, red), the multivariate assimilation using T-S covariance without salinity observations (T2TS, green) and the multivariate assimilation using both T and S observations (TS2TS, blue).

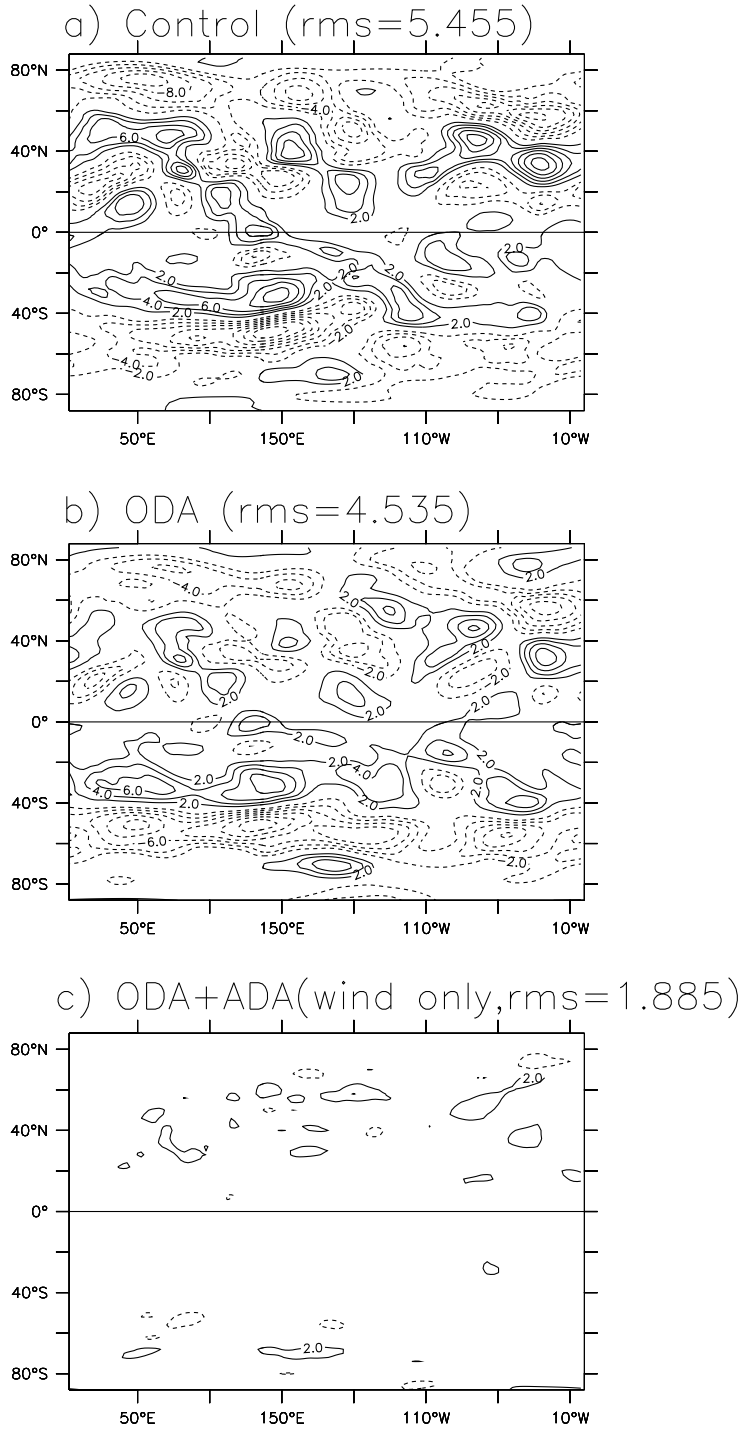

Figure 13: The atmospheric vertically-averaged zonal wind errors for (a) the control, (b) the ODA-only and (c) the case with ODA plus the atmospheric wind assimilation. The contour interval is 2 m/s. The contour 0 is omitted.

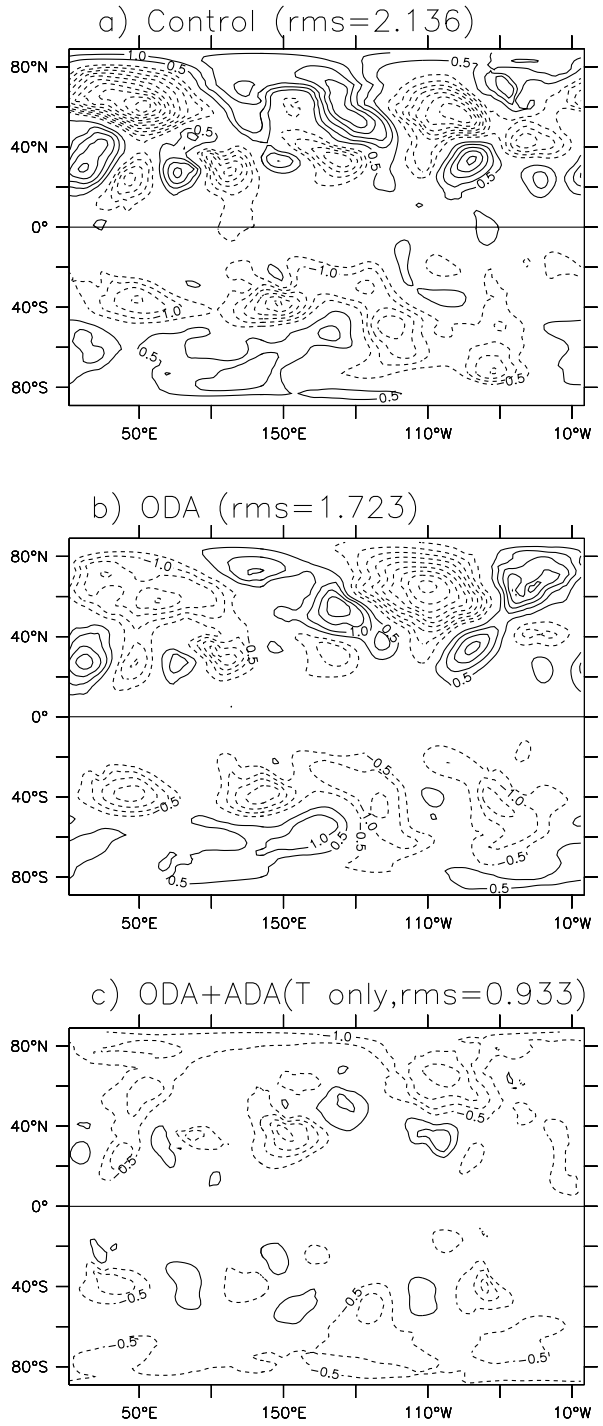

Figure 14: The atmospheric vertically-averaged temperature errors for (a) the control, (b) the ODA-only (T2TS case) and (c) the case with ODA plus the atmospheric temperature assimilation. The contour interval is 0.5°C. The contour 0 is omitted.

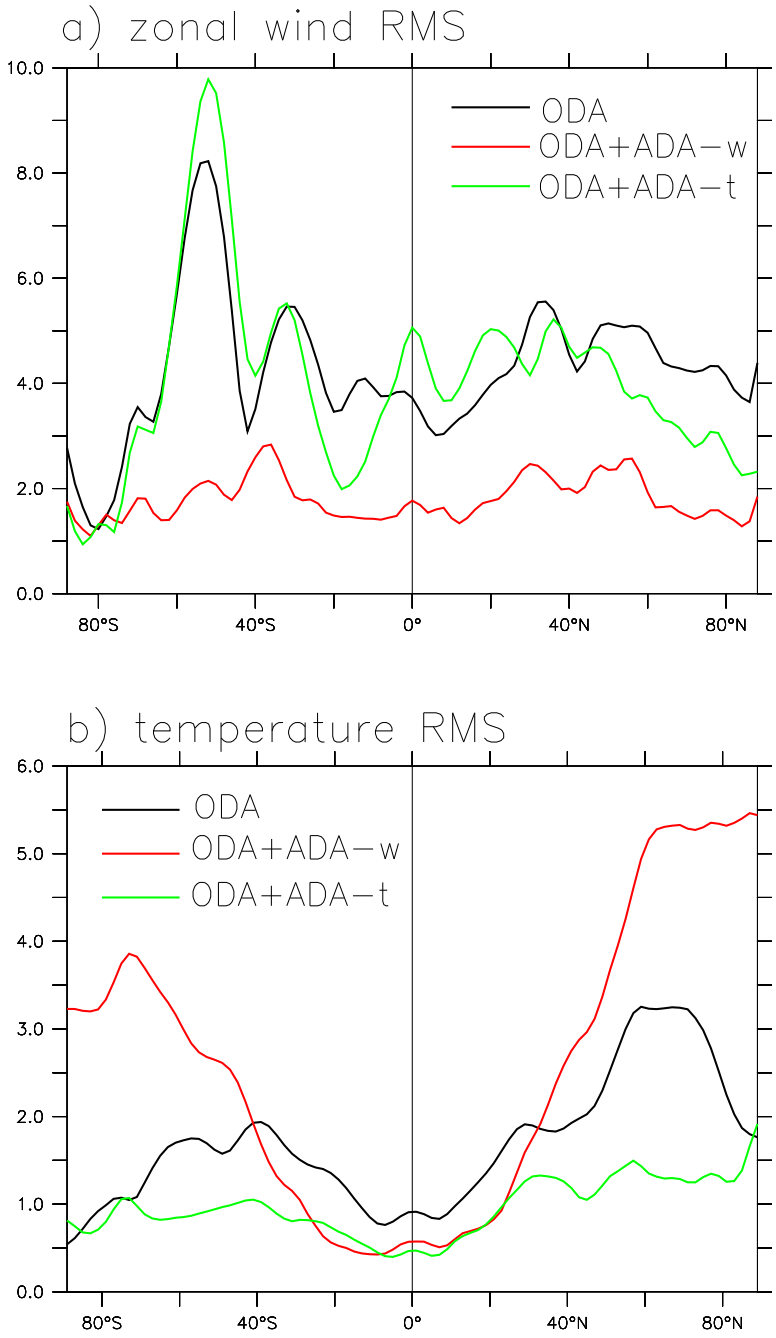

Figure 15: The RMS errors computed on zonal-vertical domain, for the atmospheric zonal wind (a) and the atmospheric temperature (b) in the ODA-only (black), the case with ODA plus the atmospheric wind assimilation (red) and the case with ODA plus the atmospheric temperature assimilation (green).

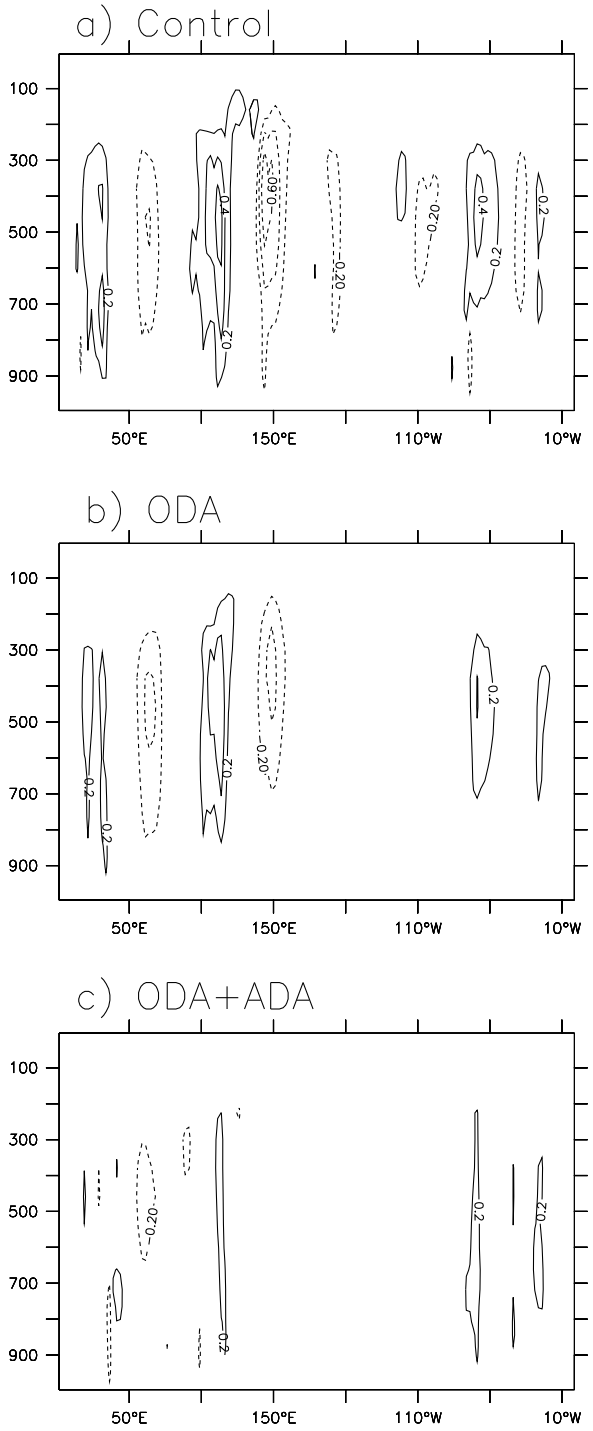

Figure 16: Vertical motion errors of the tropical atmosphere (averaged over 20^oS-20^oN for the control (a), the ODA-only (b) and ODA+ADA (c). The contour interval is 0.1 m/day. The 0-line is omitted.

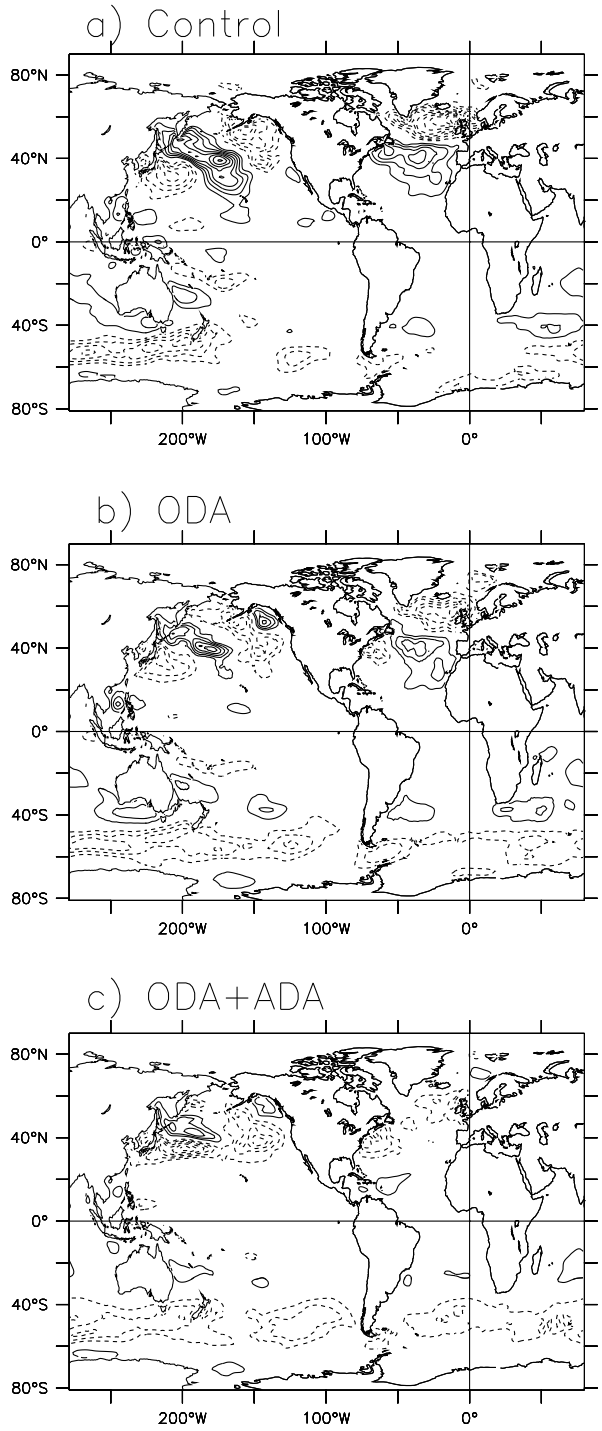

Figure 17: Zonal wind stress errors for the control (a), the ODA-only (b) and ODA+ADA (c). The contour interval is 0.04 N/m^2. The 0-line is omitted.

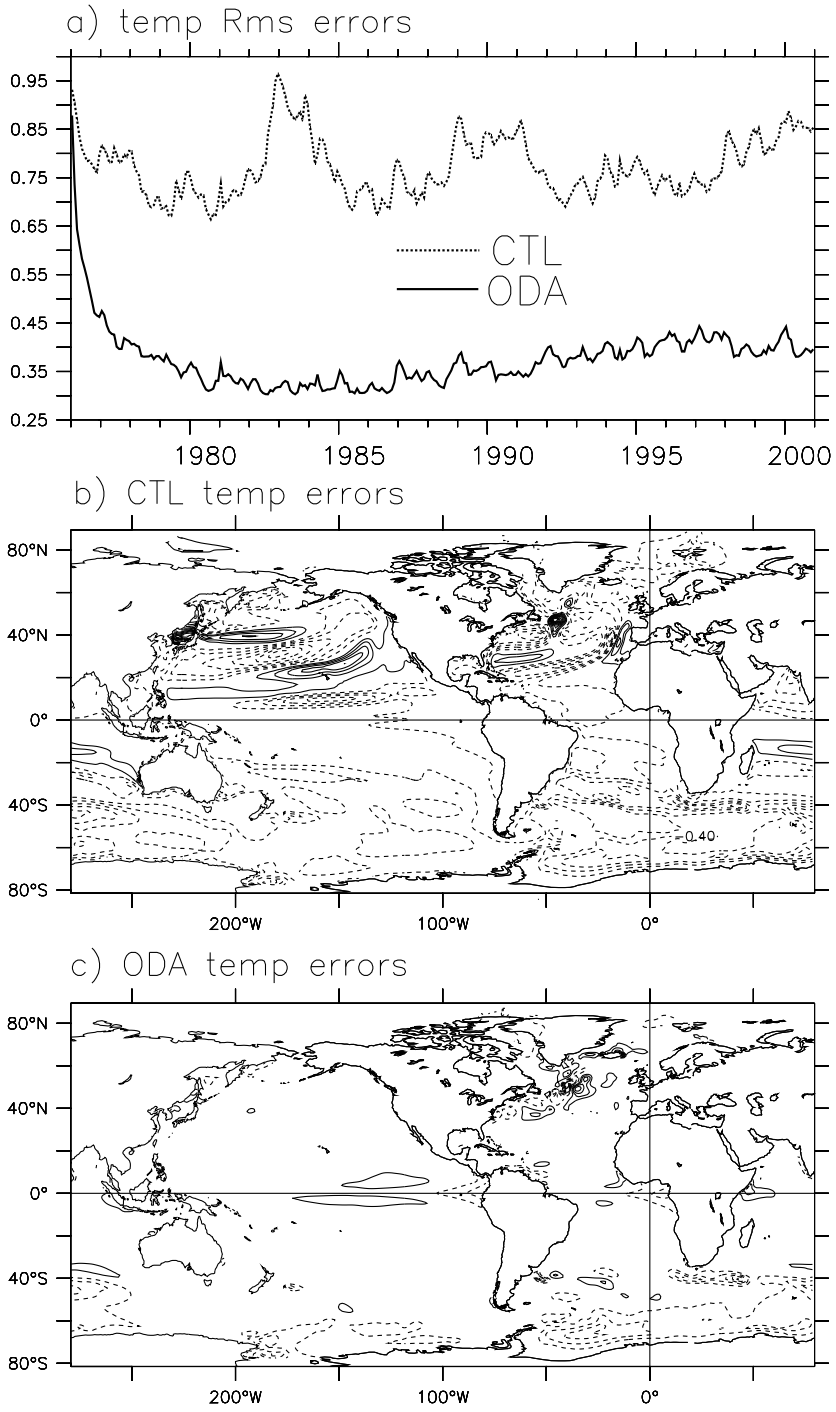

Figure 18: Timeseries of the global RMS error of the top 500 m ocean temperature (a) for the control (dotted) and the ODA (solid), and time mean of vertically-averaged ocean temperature errors over the top 500 m. The contour interval in (b) and (c) is 0.2^oC. The contour 0 is omitted.

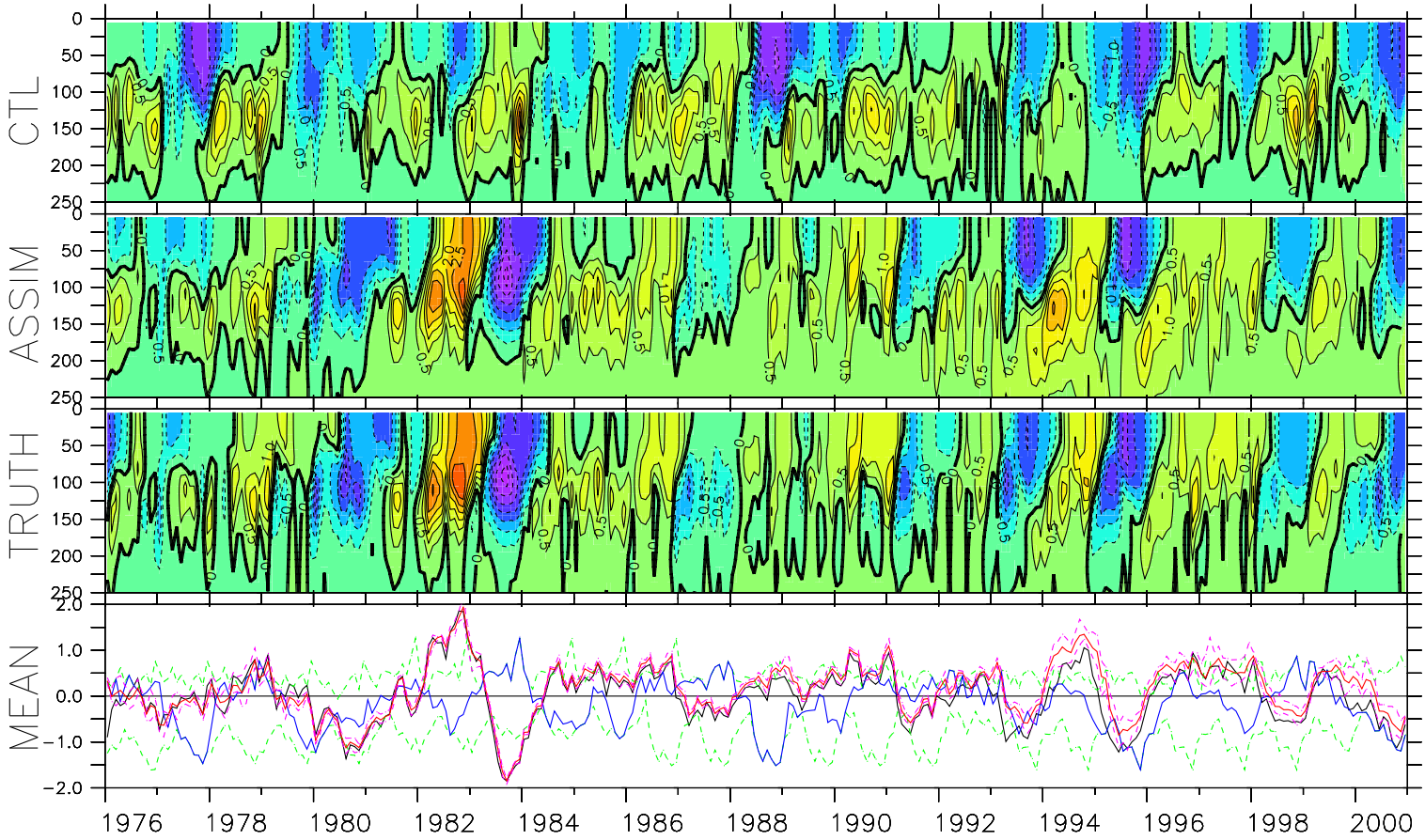

Figure 19: Timeseries of the anomalies of the Nino3.4 ocean temperature for the control (denoted by CTL), the ODA (denoted by ASSIM) and the truth. Curves in the bottom panel are the vertical averages over top 250 m for the control (blue), the ODA (red) and the truth (black). The upper and lower bounds of the control/ODA spread are plotted by the green-dashed/pink-dashed lines in the bottom panel. The control (model climatological) spread is estimated by 6 25-year non-overlap timeseries and the ODA spread is computed by 6 ensemble members in the filter. All anomalies are computed using the truth's climatology and the contour interval for the first three panels is 0.5^{o}C.

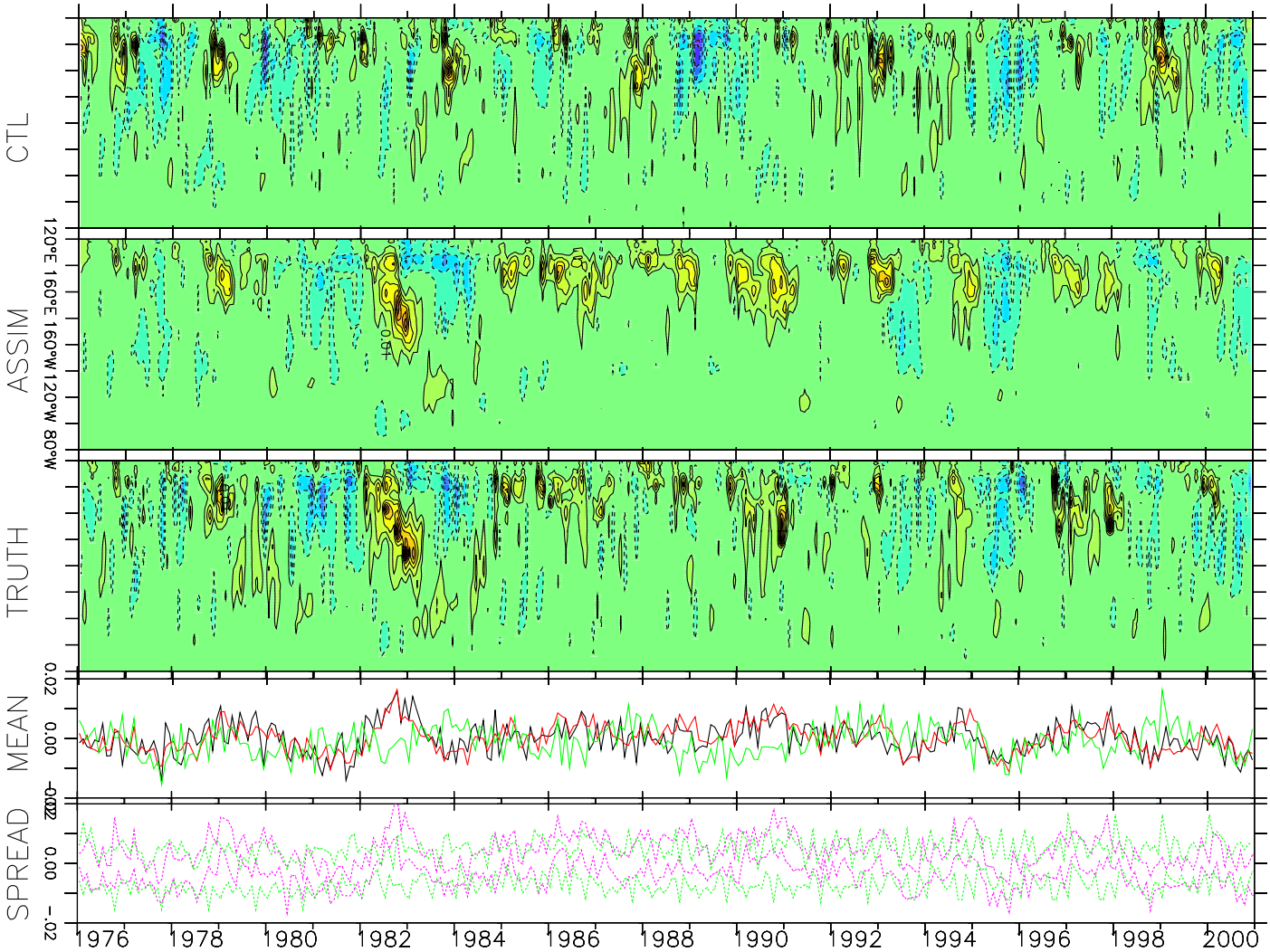

Figure 20: Timeseries of the anomalies of the zonal wind stress (τ_x) at the tropical Pacific (5^oS-5^oN average for the control (denoted by CTL), the ODA (denoted by ASSIM) and the truth. Curves in the panel next to the bottom are the zonal averages over the Pacific for the control (green), the ODA (red) and the truth (black). The upper and lower bounds of the control/ODA spread are plotted by the green-dashed/pink-dashed lines in the bottom panel. The method for estimating the spread is the same as for Fig. 19. All anomalies are computed using the truth's climatolgy and the contour interval for the first three is 0.01 N/m^2.

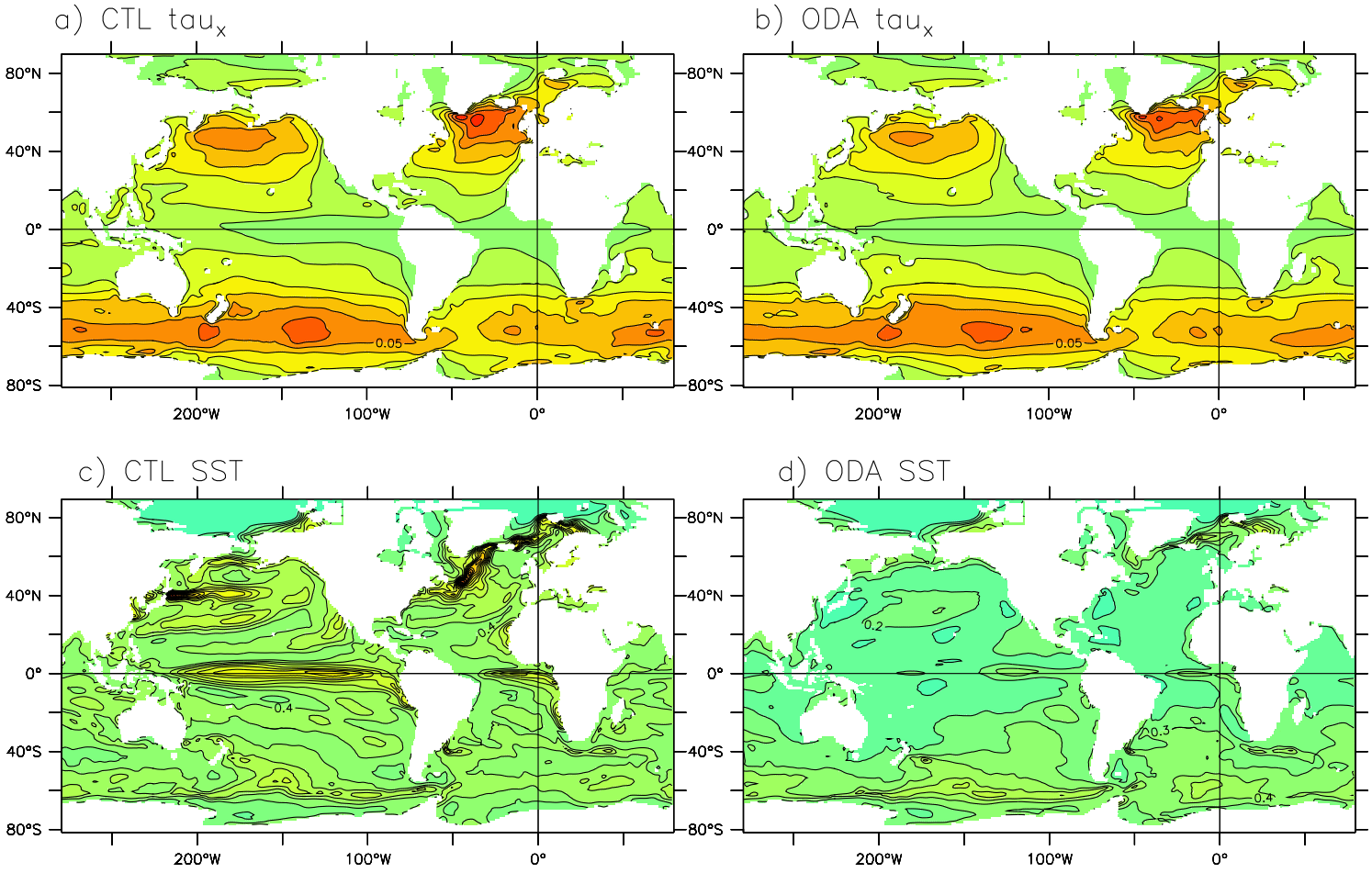

Figure 21: Time mean of the standard deviations of the zonal wind stress spread (top a, b) and the SST spread (bottom c, d) in the control (left a, c) and ODA (right b, d). The method for estimating the spread is the same as for Fig. 19. The contour interval is 0.01 N/m^2 for a, b, and 0.1^{o}C for c, d.

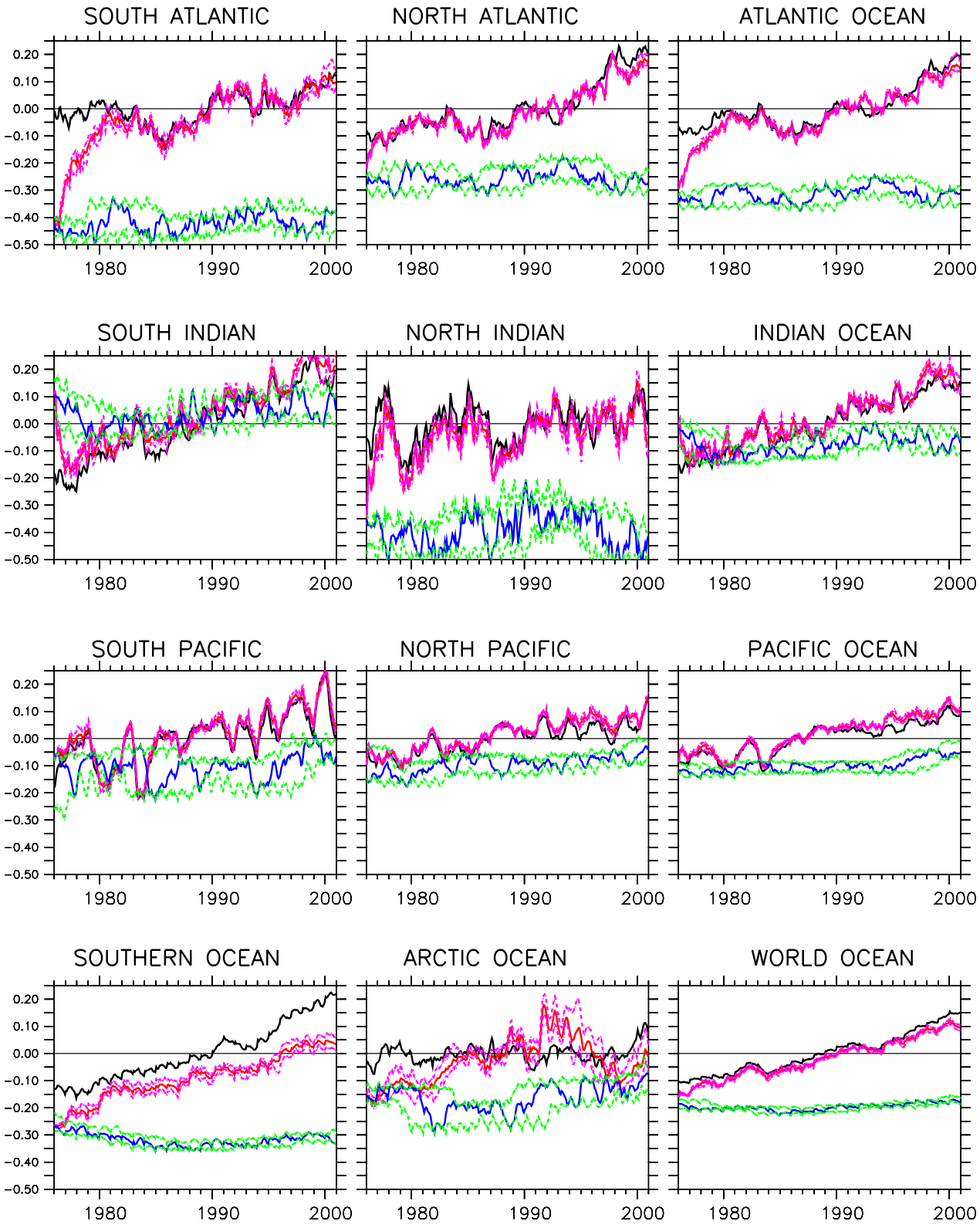

Figure 22: Timeseries of the anomalies of the top 500 m ocean heat content (averaged temperature) in different oceans for the truth (black), the ODA (red) and the control (blue). The upper and lower bounds of the control/ODA spread are plotted by the green-dashed/pink-dashed lines. The method for estimating the spread is the same as for Fig. 19. All anomalies are computed using the truth's climotolgy.